Contrib Mineral Petrol (2012) 164:157–175
DOI 10.1007/s00410-012-0731-y

ORIGINAL PAPER

The effects of solid solution and diffusion on infiltration-driven metamorphism with application to metaperidotite, Val d'Efra, Central Swiss Alps

Nathan W. Winslow · John M. Ferry

Received: 15 July 2011 / Accepted: 17 February 2012 / Published online: 7 March 2012

Abstract The complication introduced by solid solutions in the analysis of infiltration-driven mineral reactions is that the mole fraction of tracer component i in fluid (X_i) changes with reaction progress (ξ). The effect was incorporated into transport models for coupled fluid flow and mineral reaction by parameterizing the relation between X_i and ξ. With specific reference to carbonation and hydration during regional metamorphism of the peridotite body in Val d'Efra, whose constituent minerals are all solid solutions, infiltration of a disequilibrium fluid produces a single sharp reaction front if rock is assumed uniform in composition. The reaction front separates completely unreacted rock downstream from rock upstream with ξ at a steady-state limit ($\xi_{ss} \leq \xi_{max}$) that depends on input fluid composition (ξ_{max} is the maximum possible value). Novel phenomena develop, however, if the flow medium, like the metaperidotite body, is composed of many small domains that differ in initial mineral modes and compositions but with X_i homogenized at a spatial scale larger than the size of the domains (e.g., by diffusion). In this case, infiltration of a disequilibrium fluid produces up to as many different reaction fronts along the flow path as there are domains with $0 \leq \xi < \xi_{ss}$ in all domains except upstream from the slowest moving front where $\xi = \xi_{ss}$ in all domains. Measured values of ξ in the metaperidotite, (all $0 < \xi < \xi_{max}$) are best reproduced by down-temperature infiltration of a disequilibrium fluid with $X_{CO_2} = 0.196$ into a multi-domain medium with uniform X_{CO_2} at each spatial point along the flow path (homogenized across the domains at the m-scale by diffusion), and time-integrated fluid flux $\geq$1,836 mol fluid/cm^2 rock. Results resolve the paradox of the widespread spatial distribution of reactants and products of infiltration-driven decarbonation/dehydration reactions in regional metamorphic terrains (which in the absence of solid solution and compositional domains indicate up-temperature flow) and the prediction of hydrodynamic models that regional metamorphic fluid flow normally is directed vertically upward and down temperature.

Keywords Regional metamorphism · Fluid–rock interaction · Chemically reactive fluid flow · Reaction mechanisms · Reaction fronts · Time-integrated fluid flux · Diffusion · Solid solution · Metamorphosed peridotite · Val d'Efra, Swiss Alps

Introduction

Mineral reactions that were driven by the infiltration of rocks during metamorphism by chemically reactive fluids have been documented in Barrovian and Buchan regional metamorphic terrains, in contact aureoles, and in some blueschist facies terrains (e.g., reviews by Ferry and Gerdes 1998; Ferry et al. 2002; Ague 2003). A wide range of rock types may be affected, including dolomite, siliceous dolomite and limestone, marl, pelite, psammite, mafic and silicic volcanic and plutonic rock, and ultramafic rock. A fundamental question about each specific occurrence of infiltration-driven metamorphism is the mechanism of fluid–rock reaction (disequilibrium or gradient flow

Communicated by T.L. Grove.

N. W. Winslow
Raytheon BBN Technologies, 1300 North 17th Street, Arlington, VA 22209, USA

J. M. Ferry (✉)
Department of Earth and Planetary Sciences, Johns Hopkins University, Baltimore, MD 21218, USA
e-mail: jferry@jhu.edu

mechanism) and the amount of fluid involved, measured as a time-integrated fluid flux. To date, mechanisms of fluid–rock reaction and time-integrated fluid fluxes normally have been evaluated considering that minerals are fixed in composition and that the effects of hydrodynamic dispersion and CO_2-H_2O interdiffusion at a spatial scale larger than hand specimens are negligible. (For brevity, the combined effects of dispersion and diffusion will be referred to just as diffusion.) Many minerals that participate in infiltration-driven reactions, however, are solid solutions, particularly in regional metamorphic rocks. Furthermore, it is now recognized that significant CO_2-H_2O interdiffusion may occur across heterogeneities in rock composition, such as layering, during regional metamorphism at spatial scales in some cases up to 70 m (e.g., Bickle et al. 1997; Ague and Rye 1999; Ague 2000, 2002, 2003; Ferry et al. 2005; Penniston-Dorland and Ferry 2006; Ferry 2007).

This contribution explores how solid solution and diffusion affects mineral-fluid reaction in reactive fluid flow systems. In more detail, results demonstrate how the mechanism of fluid–rock reaction and time-integrated fluid flux in metamorphic rocks can be rigorously evaluated even when (1) one or more of the mineral reactants and products are solid solutions and (2) the flow medium is composed of domains of differing bulk composition that are smaller than the scale at which the composition of CO_2-H_2O fluid is homogenized by diffusion. The study specifically focuses on infiltration-driven carbonation and hydration of metaperidotite during Barrovian regional metamorphism in Val d'Efra, Central Swiss Alps, as an example.

Geological context

The metaperidotite body at Guglia, Val d'Efra (Fig. 1), is a boudin, ~30 m in diameter, primarily composed of olivine-talc-magnesite-chlorite schist (Evans and Trommsdorff 1974; the schlieren facies of Ferry et al. 2005). Schlieren are defined by dm-sized domains that differ in bulk chemical composition and hence in the relative proportions of olivine, talc, and magnesite (Fig. 2). Schlieren are flattened in the plane of the foliation. Course-grained enstatite-olivine-talc-magnesite-chlorite schist (the prismatic enstatite facies of Ferry et al. 2005) is a minor rock type that forms a thin, 1- to 2-m-thick shell around much of the margin of the metaperidotite body. Country rock is quartzo-felspathic gneiss. The present mineralogy of the metaperidotite developed during Alpine Barrovian regional metamorphism at or near temperature (T)-pressure (P) conditions recorded by mineral equilibria, 645 ± 10°C and 7 ± 1 kbar (Ferry et al. 2005). Olivine, talc, and magnesite are for practical purposes Fe–Mg solid solutions with idealized formulas. Magnesite developed during Barrovian metamorphism by the reaction,

$$4\underset{\text{olivine}}{(\mathrm{Mg,Fe})\mathrm{SiO_4}} + 5\ \mathrm{CO_2} + \ \mathrm{H_2O} = \underset{\text{talc}}{(\mathrm{Mg,Fe})_3\mathrm{Si_4O_{10}(OH)_2}} + 5\underset{\text{magnesite}}{(\mathrm{Mg,Fe})\mathrm{CO_3}}, \quad (1)$$

driven by infiltration of an olivine-talc-chlorite precursor by CO_2-H_2O fluid (Evans and Trommsdorff 1974; Ferry et al. 2005). All samples of the schlieren facies contain both reactants and products of reaction (1). Progress (ξ) of reaction (1) (with units of mol/cm^3 rock) varies by a factor of ~2.5 along a ~1 m traverse across the schlieren facies oriented perpendicular to foliation and the long dimensions of the schlieren (Fig. 3, Table 1). Olivine in the samples is uniform in composition within error of measurement (weighted mean mole fraction of the forsterite component, $X_{fo} = 0.888 \pm 0.001$). The uniformity in X_{fo} along the traverse is interpreted as equilibration of all rocks with a CO_2-H_2O fluid whose mole fraction of CO_2 (X_{CO_2}) was efficiently homogenized during metamorphism by CO_2-H_2O interdiffusion at the scale of the traverse (Ferry et al. 2005). The goal of the study was to develop transport models of coupled fluid flow and mineral-fluid reaction that reproduce the measured values of ξ in Fig. 3 under the constraint of uniform fluid composition during reaction (1) along the traverse.

Phase equilibrium calculations

When mineral reactants and products are fixed in composition, equilibrium X_{CO_2} during an infiltration-driven carbonation/hydration (or decarbonation/dehydration) reaction is constant at a given spatial point in the flow system at constant P and T. The complication introduced by solid solutions is that X_{CO_2} at a given spatial point varies with ξ even if P and T are constant. One approach to the problem is to approximate a solid solution as a large set of discrete compounds of fixed composition spanning the relevant range of each solid solution series (Lichtner and Carey 2006). Because the essence of the complication introduced by solid solution is that X_{CO_2} becomes a function of ξ, an alternative approach is simply to parameterize ξ-X_{CO_2} relations for input to any transport calculation. This was accomplished in the case of the Val d'Efra metaperidotite by the development of a quantitative model for reaction (1) for 13 samples along the ~1-m-long traverse. Four other samples collected along the traverse (I, L, L1, M) that contain small amounts of enstatite (≤4 modal %) were ignored because the role of fluid–rock reaction in the formation of enstatite is uncertain. Ignoring the four samples

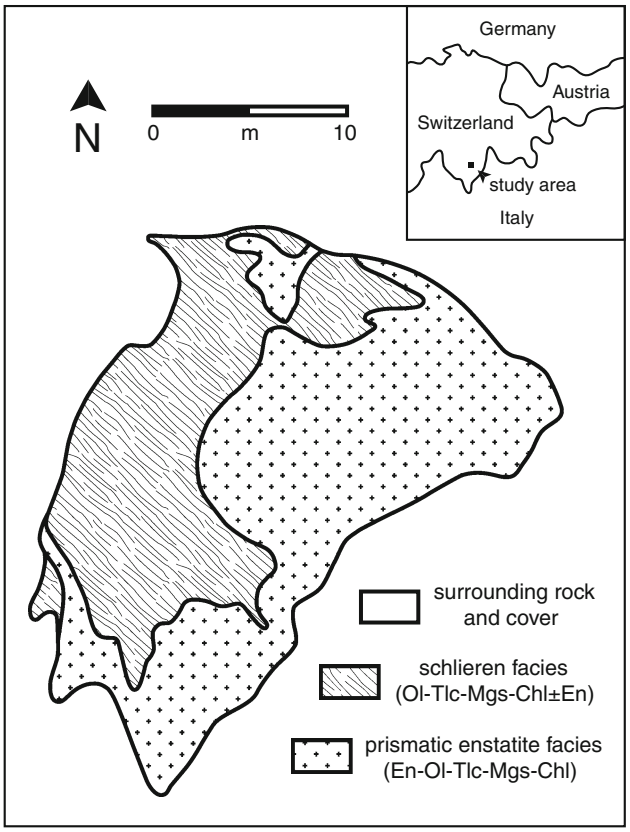

Fig. 1 Geologic map of the metaperidotite body at Guglia, Val d'Efra, Central Alps, Switzerland (from Ferry et al. 2005). Body is located on the Osogna 1:25 000 topographic map at 708.9/132.38 (Swiss national grid). *Ol,* olivine; *Tlc,* talc; *Mgs,* magnesite; *Chl,* chlorite; *En,* enstatite

Fig. 2 Schlieren facies of the metaperidotite body at Guglia, Val d'Efra. Knife handle is 9 cm long. The exposure is oblique to foliation and the long dimensions of the schlieren. *Light-colored* areas contain more talc and less olivine than surrounding *dark* matrix

is justified both because of the small amount of enstatite in them and because 80% of the samples collected from the schlieren facies in the metaperidotite body contain no

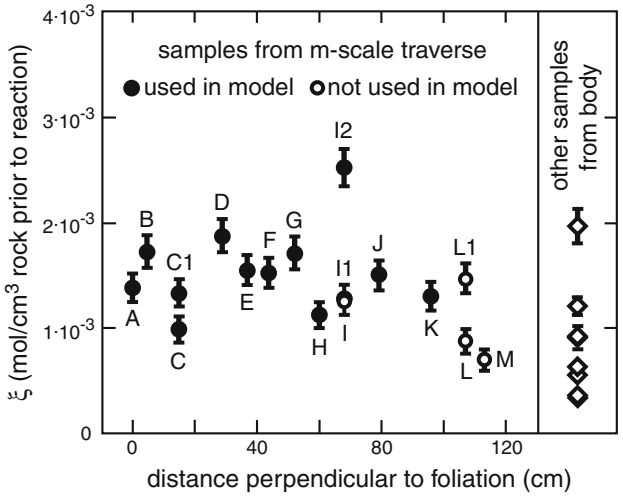

Fig. 3 Values of the progress of reaction (1) in all analyzed samples from the schlieren facies, with reference to 1 cm^3 of rock prior to initiation of the reaction (from Ferry et al. 2005). Sample designation is the same as in Table 1. *Error bars* represent ±2 SD based on the statistics of point pointing (error bar not displayed when smaller than the size of the *symbol*). Measured values were corrected for the occurrence of serpentine in all samples and of enstatite in five samples (Ferry et al. 2005). Results in the left-hand panel refer to samples collected along a traverse perpendicular to foliation and the long dimensions of the schlieren. Results in the right-hand panel refer to all other samples collected of the schlieren facies. Transport models of coupled fluid flow and mineral-fluid reaction are developed in this paper to quantitatively reproduce values of ξ in all samples along the traverse excluding those that contain small amounts (≤4 modal %) of enstatite (samples I, L, L1, M)

enstatite. Using measured modes, empirical Fe–Mg exchange coefficients, and the present weighted mean $X_{fo} = 0.888$, the amounts and compositions olivine and talc in the olivine-talc-chlorite precursor to each sample prior to reaction (1) were computed following Ferry et al. (2005) and Penniston-Dorland and Ferry (2006). Results are listed in Table 1. Differences in amounts and compositions of olivine and talc among the precursors prove that observed variations in the amounts olivine, talc, and magnesite in the schlieren facies are due to differences in bulk compositions of the precursors as well as to variations in ξ. Amounts and compositions of olivine, talc, and magnesite per unit volume of the precursor were then calculated at increments of ξ up to the maximum value at which all olivine is consumed. Values of X_{CO_2} were computed at each increment of ξ from the equilibrium among olivine, talc, magnesite, and CO_2-H_2O fluid using the Berman (1988, updated June 1992) database and the Kerrick and Jacobs (1981) equation of state for CO_2-H_2O fluid, and assuming ideal ionic mixing of Fe and Mg in the minerals. Results for three representative samples with reaction at 7 kbar and 645°C are illustrated as circles in Fig. 4. The ξ- X_{CO_2} relations for samples C and I2 bracket those for the other 11 samples (sample J is an example).

Table 1 Selected data for samples of carbonated metaperidotite from Val d'Efra

Samples/ Domains[a]	Volume Fraction[b]	Measured ξ (mol/cm^3)[c]	$n°$(olivine) (mol/cm^3)[d]	$n°$(talc) (mol/cm^3)[d]	$X°_{Fe}$(olivine)[e]	$X°_{Fe}$(talc)[e]	Maximum ξ (mol/cm^3)[f]	X_{CO_2} at start of reaction[g]	X_{CO_2} at end of reaction[g]
A	0.048	$1.38\ (0.14) \times 10^{-3}$	1.732×10^{-2}	1.094×10^{-3}	0.0921	0.019	4.33×10^{-3}	0.1884	0.2348
B	0.072	$1.73\ (0.15) \times 10^{-3}$	1.960×10^{-2}	0.475×10^{-3}	0.0895	0.018	4.90×10^{-3}	0.1875	0.2347
C	0.058	$0.99\ (0.12) \times 10^{-3}$	1.688×10^{-2}	1.380×10^{-3}	0.0973	0.020	4.22×10^{-3}	0.1904	0.2399
C1	0.058	$1.34\ (0.13) \times 10^{-3}$	1.814×10^{-2}	0.878×10^{-3}	0.0935	0.019	4.54×10^{-3}	0.1889	0.2369
D	0.106	$1.88\ (0.15) \times 10^{-3}$	1.663×10^{-2}	1.478×10^{-3}	0.0839	0.017	4.16×10^{-3}	0.1854	0.2266
E	0.072	$1.55\ (0.15) \times 10^{-3}$	1.882×10^{-2}	0.746×10^{-3}	0.0912	0.019	4.70×10^{-3}	0.1881	0.2355
F	0.072	$1.53\ (0.14) \times 10^{-3}$	1.345×10^{-2}	2.543×10^{-3}	0.0846	0.017	3.36×10^{-3}	0.1857	0.2241
G	0.077	$1.72\ (0.15) \times 10^{-3}$	1.581×10^{-2}	1.924×10^{-3}	0.0850	0.017	3.95×10^{-3}	0.1858	0.2272
H	0.077	$1.13\ (0.12) \times 10^{-3}$	1.408×10^{-2}	2.358×10^{-3}	0.0925	0.019	3.52×10^{-3}	0.1886	0.2322
I1	0.046	$1.29\ (0.13) \times 10^{-3}$	1.536×10^{-2}	2.010×10^{-3}	0.0918	0.019	3.84×10^{-3}	0.1883	0.2332
I2	0.046	$2.52\ (0.18) \times 10^{-3}$	1.989×10^{-2}	0.422×10^{-3}	0.0797	0.016	4.97×10^{-3}	0.1839	0.2248
J	0.134	$1.50\ (0.14) \times 10^{-3}$	1.700×10^{-2}	1.341×10^{-3}	0.0901	0.018	4.25×10^{-3}	0.1877	0.2327
K	0.134	$1.31\ (0.13) \times 10^{-3}$	1.401×10^{-2}	2.184×10^{-3}	0.0895	0.018	3.50×10^{-3}	0.1875	0.2288

[a] From Ferry et al. (2005) with the "16" prefix omitted for brevity

[b] With respect to the m-scale traverse across the metaperidotite body in Fig. 3

[c] Reaction progress with reference to 1 cm^3 rock prior to reaction (1) (Ferry et al. 2005). Numbers in parentheses are 2 SD uncertainties estimated from point counting statistics

[d] moles olivine and talc in 1 cm^3 rock prior to reaction

[e] Fe/(Fe + Mg) of olivine and talc in rock prior to reaction

[f] Calculated reaction progress if reaction (1) were to go to completion

[g] Mole fraction of CO_2 in fluid when reaction (1) starts or goes to completion at 645°C and 7 kbar, calculated from phase equilibria

Calculated results, represented by the circles in Fig. 4, were parameterized as input to transport calculations by fitting X_{CO_2} to ξ with either a quadratic equation or a cubic equation depending on the requirements of the computation. Even the poorer quadratic fits deviate from the phase equilibrium calculations by ≤ 0.0014 X_{CO_2} within the region of fit (Fig. 4). In some transport calculations in which only X_{CO_2} at the start of reaction ($\xi = 0$) was needed, that value was taken directly from the phase equilibrium calculations.

Transport calculations: assumptions and specifications

The transport calculations involve assumptions and specifications that anticipate their application to metamorphism of the peridotite body in Val d'Efra: (1) mineral-fluid equilibrium was assumed at all times during mineral-fluid reaction, (2) the only volatiles involved in the reaction are CO_2 and H_2O, (3) fluid is a CO_2-H_2O solution, and (4) the tracer component is CO_2. These allow results of the calculations additionally to be directly compared to calculations in other publications that made the same assumptions and specifications but that considered that mineral reactants and products were fixed in composition and that the effects of diffusion were negligible. The assumption of mineral-fluid equilibrium, in particular, was adopted so that the effects of solid solution would not be confused with additional effects introduced by a kinetically controlled mineral-fluid reaction.

Transport calculations: models of the disequilibrium flow mechanism

Disequilibrium flow refers to the case where rock is infiltrated by a fluid that initially is out of chemical equilibrium with rock at the inlet and further downstream. The transport calculations consider a one-dimensional flow system with distance coordinate, z, that increases downstream, in most calculations from a value of 0 at the inlet to the flow system.

Sharp or broad reaction fronts in a homogeneous medium?

When mineral reactants and products are fixed in composition, disequilibrium flow produces a sharp reaction front that separates completely reacted rock upstream that is in equilibrium with the input fluid from completely unreacted

rock downstream (Ferry 1991). As flow proceeds, the reaction front propagates downstream as a step-function in ξ across which ξ changes from 0 downstream to the maximum value, ξ_{max}, on the upstream side. At constant P and T, the rate of advance of the reaction front with respect to input of reactive fluid is derived from a mass balance equation for tracer component i (Ferry 1991):

$$X^{eq} = \frac{X^{\circ}q^{\circ} + \nu_i \xi_{max} z(F)}{q^{\circ} + \Sigma \nu_j \xi_{max} z(F)}, \quad (2)$$

where X° and X^{eq} are the mole fraction of i in the input fluid and of fluid in equilibrium with reactants and products at the reaction front, respectively; q° is the molar time-integrated flux of input fluid (with units of mol fluid/cm^2 rock); $z(F)$ is the distance that the reaction front then moves downstream (in cm); ν_i is the stoichiometric coefficient of i in the reaction (positive for products and negative for reactants); and $\Sigma \nu_j$ is the sum of the coefficients of all fluid species involved in the reaction (including i). Taking CO_2 as the tracer component, and applying Eq. 2 specifically to reaction (1),

$$\frac{z(F)}{q^{\circ}} = v(F) = \frac{X^{eq} - X^{\circ}}{[\nu_{CO_2} - X^{eq}(\nu_{CO_2} + \nu_{H_2O})]\xi_{max}} = \frac{X^{\circ} - X^{eq}}{(5 - 6X^{eq})\xi_{max}}, \quad (3)$$

where $v(F)$ is the "velocity" of advance of the reaction front, using input of time-integrated fluid flux as a proxy for time. Because Eq. 3 defines a linear relation between q° and $z(F)$, $v(F)$ is constant. Reaction (1) specifically proceeds only if $X^{\circ} > X^{eq}$. If $X^{\circ} \leq X^{eq}$, input fluid is initially in equilibrium with rock everywhere in the flow system and no reaction occurs.

The record of disequilibrium flow in the field then is the occurrence of reaction fronts that separate completely reacted from completely unreacted rocks (e.g., Cook and Bowman 2000; Ferry et al. 2001). In contrast, widespread occurrence of rocks with both reactants and products of an infiltration-driven reaction ($0 < \xi < \xi_{max}$) is a record of the gradient flow reaction mechanism if minerals are fixed in composition (Baumgartner and Ferry 1989; Ferry 1991). If mineral reactants and products are solid solutions, however, the disequilibrium flow mechanism can produce either sharp or broad reaction fronts depending on how fluid composition changes with ξ (Hofmann 1972). A widespread occurrence of coexisting reactants and products that are solid solutions with $0 < \xi < \xi_{max}$, such as in the metaperidotite at Val d'Efra (Fig. 3, Table 1), therefore, in principle, could have been produced by either the disequilibrium flow or the gradient flow mechanism.

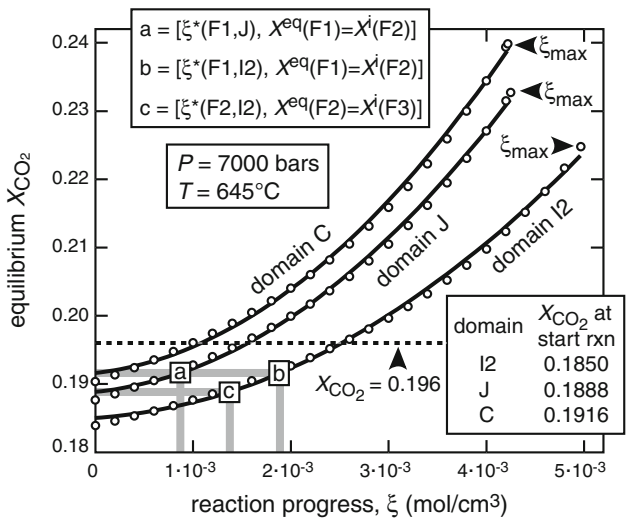

Fig. 4 Dependence of X_{CO_2} on progress (ξ) of reaction (1), calculated from phase equilibria as described in the text (*open circles*). Results for domains/samples I2 and C bracket results for all others in Table 1 (J is an example). *Solid curves* are quadratic fits to results of the phase equilibrium calculations. The horizontal *dotted line* represents X_{CO_2} of fluid in equilibrium with all samples along the traverse in Fig. 3 at 645°C and 7 kbar. Values of ξ^* in the top inset for points *a*, *b*, and *c* in the figure refer to quantities defined in Fig. 6. Values of X_{CO_2} at the start of reaction for the three domains/samples (bottom inset) are taken from the quadratic fits

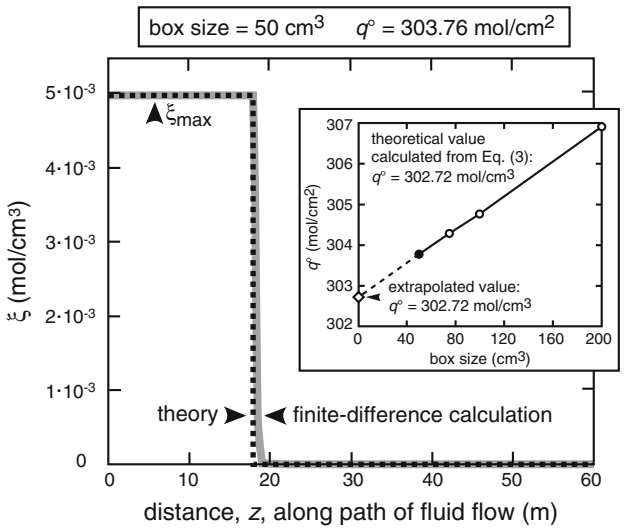

Fig. 5 Reaction front developed by infiltration of homogeneous model metaperidotite with CO_2-H_2O fluid of composition $X_{CO_2} = 0.3$. Temperature (645°C) and P (7 kbar) are constant along the flow path. The initial compositions and abundances of minerals are the same as in sample I2, Table 1. *Black dashed line* is the reaction front expected from theory; *solid gray line* is the front calculated by the finite-difference method. In both cases, the front is displaced 18 m from the inlet to the flow system at $z = 0$. Inset shows the time-integrated input fluid flux (q°) needed to displace the reaction front 18 m, estimated from the finite-difference method using box sizes of 50, 75, 100, and 200 cm^3 (*black circle* indicates *box* size used to calculate the reaction front represented by the *solid gray line*). Extrapolation of calculated q° to zero box size (*open diamond*), using results for the 50 and 75 cm^3 *boxes*, gives a value the same within error as that obtained from Eq. 3

According to chromatographic theory (Hofmann 1972), a sharp reaction front is produced when minerals are solid solutions if the slowest moving fluid composition is the initial one when reaction just begins (i.e., at $\xi = 0$). Upstream from the reaction front, where rock is in equilibrium with the input fluid, ξ has a steady-state value (ξ_{ss}) in the range $0 < \xi_{ss} \leq \xi_{max}$, depending on X°. For example, considering a medium with the same composition as sample I2, Table 1, no reaction front develops if $X^\circ \leq 0.184$ (Fig. 4, Table 1). If $0.184 < X^\circ < 0.225$, $0 < \xi_{ss} < \xi_{max}$, with ξ_{ss} increasing with increasing X° (Fig. 4). Only if $X^\circ > 0.225$ is $\xi_{ss} = \xi_{max}$ (Fig. 4).

The rate of advance of a sharp reaction front can be calculated from Eq. 3 when minerals are solid solutions by replacing ξ_{max} with $\xi_{ss} \leq \xi_{max}$. The dashed line in Fig. 5 illustrates, as an example, the sharp reaction front that would develop in rock specifically with mineralogy and mineral compositions the same as in the olivine-talc-chlorite precursor to sample I2 (Table 1) when it is infiltrated by fluid with $X^\circ = 0.3$ at 645°C and 7 kbar. Because $X^\circ > 0.225$, $\xi_{ss} = \xi_{max}$. The velocity of the front is specified from Eq. 3 by setting X^{eq} to the value at $\xi = 0$ (0.1850, taken from the quadratic fit to the ξ-X^{eq} data in Fig. 4) and $\xi_{max} = 4.97 \times 10^{-3}$ mol/cm^3 (Table 1). The dashed line illustrates the front after it has migrated 18 m downstream from the inlet to the flow system ($z = 0$). The displacement was chosen as a length comparable to the dimension of the metaperidotite body in Val d'Efra. From Eq. 3, the required time-integrated input fluid flux, q°, is 302.72 mol/cm^2.

Calculations based on a finite-difference model of the flow system confirm that infiltration of chemically homogeneous metaperidotite by fluid with $X^\circ = 0.3$ actually does produce a single sharp reaction front (Winslow 2009). The finite-difference model considers one-dimensional flow along distance coordinate z that increases in the direction of flow. The medium is divided into boxes with 1 cm^2 area perpendicular to flow. The lengths of the boxes along the flow path were varied between 50 and 200 cm to evaluate the effect of box size on calculated results. The medium is considered to be metaperidotite initially composed of olivine-talc-chlorite rock that experiences reaction (1) when infiltrated by CO_2-H_2O fluid of appropriate initial composition (X°) at the inlet to the flow system. For convenience of calculation, fluid is introduced in pulses in an amount that corresponds to 1% porosity. The molar time-integrated fluid flux of each pulse at the inlet (Δq°), therefore, is $0.01(V_{box})/(\overline{V}^\circ_{fluid})$, where V_{box} is the volume of the box, and $\overline{V}^\circ_{fluid}$ is the molar volume of the fluid at the inlet. Considering the jth pulse and the kth box, the increment of time-integrated flux and composition of fluid entering the upstream end are, respectively, $\Delta q^i_{j,k}$ and $X^i_{j,k}$. Fluid then equilibrates with model metaperidotite, resulting in an incremental amount of progress of reaction (1), $\Delta\xi_{j,k}$; a new fluid composition in equilibrium with the rock, $X^{eq}_{j,k}$; and new time-integrated fluid flux, $\Delta q_{j,k}$. Values of $X^{eq}_{j,k}$, $\Delta\xi_{j,k}$, and $\xi_{j,k}$ were calculated by solving three simultaneous equations. The first equation is an expression for mass balance of CO_2 based on Eq. 2:

$$X^{eq}_{j,k} = \frac{X^i_{j,k}\Delta q^i_{j,k} - 5\Delta\xi_{j,k}z_{box}}{\Delta q^i_{j,k} - 6\Delta\xi_{j,k}z_{box}}, \tag{4}$$

where z_{box} is the length of the box along the flow path. The second equation,

$$X^{eq}_{j,k} = a + b\left(\xi_{j-1,k} + \Delta\xi_{j,k}\right) + c\left(\xi_{j-1,k} + \Delta\xi_{j,k}\right)^2, \tag{5}$$

is a quadratic fit to the ξ-X^{eq} relations calculated from phase equilibria (e.g., solid curves, Fig. 4), and $\xi_{j-1,k}$, is the value of ξ in the kth box after input of $j - 1$ increments of time-integrated fluid flux. The ξ-X^{eq} relations are considered the same in every box. The third equation relates $\xi_{j,k}$, $\xi_{j-1,k}$, and $\Delta\xi_{j,k}$:

$$\xi_{j,k} = \Delta\,\xi_{j,k} + \xi_{j-1,k} = \Delta\,\xi_{j,k} + \sum_{i=1}^{j-1}\Delta\,\xi_{i,k} \tag{6}$$

($\xi_{0,k} = 0$ in all boxes). After equilibration, the increment of time-integrated flux, $\Delta q_{j,k}$, is:

$$\Delta q_{j,k} = \Delta q^i_{j,k} - 6\left(\Delta\xi_{j,k}\right)(z_{box}). \tag{7}$$

When the increment of input fluid has equilibrated in the box, the fluid is transferred to the next box downstream, where the calculation is repeated. Therefore, $X^i_{j,k}$=$X^{eq}_{j,k-1}$, $\Delta q^i_{j,k} = \Delta q_{j,k-1}$, $X^i_{j,1} = X^\circ$, and $\Delta q^i_{j,1} = \Delta q^\circ$. After a pulse of fluid traverses the entire flow system, a new pulse is introduced at the inlet and the entire procedure repeated. After m pulses of fluid have been introduced at the inlet to the flow system, the total time-integrated input fluid flux, q°, is $m\Delta q^\circ$. When reaction progress has reached the steady-state value in a box, any additional increment of introduced fluid does not react with rock in the box but proceeds downstream until it encounters a box in which $\xi < \xi_{ss}$.

Results of a finite-difference calculation for a homogeneous medium that initially has mineralogy and mineral compositions the same as the olivine-talc-chlorite precursor to sample I2 (Table 1) and is infiltrated by fluid with $X^\circ = 0.3$ at 645°C and 7 kbar are illustrated in Fig. 5. Box size is 50 cm. Increments of time-integrated fluid flux were introduced at the inlet ($z = 0$) until $\xi_{ss} = \xi_{max}$ was attained in the box whose downstream end lies at $z = 18$ m. At this point, $q^\circ = 303.76$ mol/cm^2. The gray curve shows values of ξ at all other spatial positions of the model flow system.

The agreement between calculations based on Eq. 3 and the finite-difference calculations is good but not perfect. First, the reaction front computed from the finite-difference model is steep but not exactly a step-function. Second, estimates of q° necessary to advance the reaction front 18 m from Eq. 3 and from numerical simulation are slightly different. Repetition of the finite-difference calculations at larger box size (75, 100, 200 cm) confirms that the broadening of the reaction front is an artifact of the method (numerical dissipation) that increases with increasing box size. The estimated q° necessary to advance the reaction front 18 m also increases with increasing box size (inset to Fig. 5). The equivalence of the calculations based on Eq. 3 and the finite-difference calculations in the limit of zero box size was demonstrated empirically by linearly extrapolating the trend of decreasing q° with decreasing box size to zero, specifically using results for 50- and 75-cm-long boxes (inset to Fig. 5). For each box size, uncertainty in q° from the finite-difference calculation is one pulse of input fluid (0.0183 mol for 50 cm boxes). The extrapolated value of q° in Fig. 5 therefore is uncertain by 0.06 mol/cm^2 and agrees with the theoretical prediction (Eq. 3) within error of the finite-difference method. Sharp fronts with velocities predicted by Eq. 3 develop if compositions of metaperidotite corresponding to the other 12 samples in Table 1 are considered as well.

Sharp reaction fronts in a heterogeneous medium

The metaperidotite body at Val d'Efra, however, is not uniform in composition. It is composed of numerous dm-sized domains that differed in the amounts and compositions of minerals prior to reaction (Table 1) and that appear to have equilibrated with the same fluid composition during metamorphism, likely because of diffusion (Ferry et al. 2005). Models, therefore, were developed of the disequilibrium flow mechanism for media composed of domains that differ in composition. Individual domains are considered to have ξ-X^{eq} relations like those in Fig. 4 that lead to sharp reaction fronts. The domains at each spatial point in the flow system are considered in equilibrium with fluid of the same composition. The models do not explicitly consider the effects of diffusion. Rather, the effects are implied by assuming that diffusion among domains homogenizes fluid composition to a uniform value at each spatial point at all times during mineral-fluid reaction. In nature, the domains commonly would correspond to layers that strike parallel to the direction of flow. In principle, however, the domains can have any geometry provided that (1) the spatial scale of differences in rock composition perpendicular to the flow direction is smaller than the scale at which fluid composition is homogenized by diffusion and (2) the bulk composition of the domains is the same parallel to the direction of fluid flow.

When minerals are solid solutions and the flow medium is composed of many small domains of different chemical composition, the value of ξ_{ss} in rock in equilibrium with input fluid upstream from the reaction front (or the slowest moving front if there are more than one) is more complicated. Five possible circumstances may develop depending on the value of X°. With specific reference to reaction (1), if X° is less than or equal to that of fluid in equilibrium with every domain when reaction begins, fluid infiltration does not drive reaction anywhere along the flow path, and no reaction front develops. In the case of a medium composed of three domains the same as the samples in Fig. 4, for example, no reaction occurs in domains C, I2, and J if $X^\circ \leq 0.184$ (Table 1, Fig. 4). Second, when X° is greater than that in equilibrium with some but not all domains when they begin reaction, $0 < \xi_{ss} \leq \xi_{max}$ in some domains and $\xi_{ss} = 0$ in the others. In the case of a medium composed of samples C, I2, and J, if $X^\circ = 0.186$, for example, $0 < \xi_{ss} < \xi_{max}$ in domain I2 and $\xi_{ss} = 0$ in domains C and J (Fig. 4, Table 1). Third, if X° is both greater than that at which reaction begins and less than that at which reaction is complete in every domain, $0 < \xi_{ss} < \xi_{max}$ in all domains

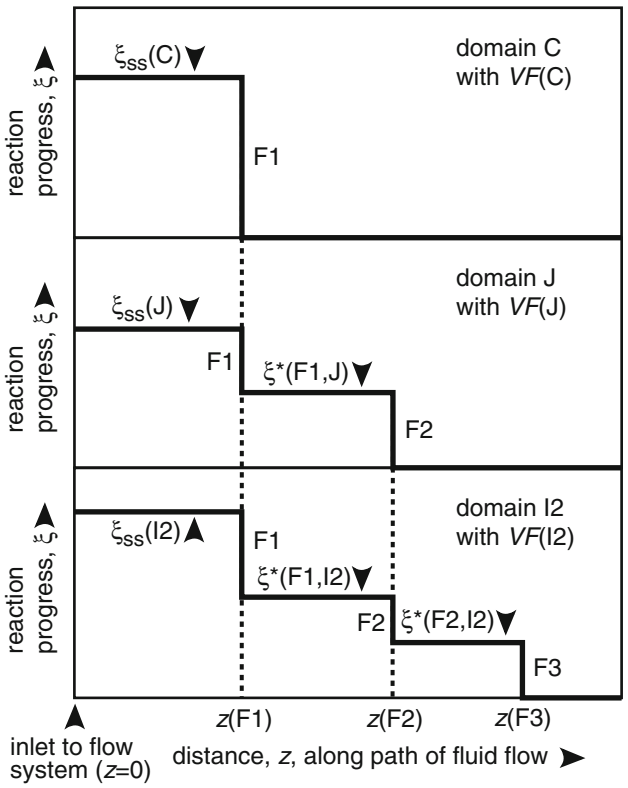

Fig. 6 Explanation of notation used in Eqs. 11–16 that describe the development of infiltration-driven reaction fronts in a medium composed of three domains with different initial modes and mineral compositions

(e.g., if $X^\circ = 0.196$, in the case of domains C, I2, and J in Fig. 4 and Table 1). Fourth, when X° is greater than the value at which reaction goes to completion in some but not all domains, $0 < \xi_{ss} < \xi_{max}$ in some domains and $\xi_{ss} = \xi_{max}$ in the others. In the case of a medium composed of samples C, I2, and J, if $X^\circ = 0.235$, for example, $0 < \xi_{ss} < \xi_{max}$ in domain C and $\xi_{ss} = \xi_{max}$ in domains I2 and J (Fig. 4, Table 1). Fifth, if X° is greater than or equal to the value at which reaction is complete in all domains, $\xi_{ss} = \xi_{max}$ in all domains (e.g., if $X^\circ \geq 0.240$, in the case of domains C, I2, and J in Fig. 4 and Table 1).

Theoretical analysis of reaction fronts in a heterogeneous medium

The behavior of a three-domain flow system is presented in a form that can be adapted to both more and fewer domains. Depending on the relative volume of the domains, up to as many reaction fronts develop as there are different domains. Figure 6 schematically illustrates the hypothetical case of a medium composed of three domains in which three reaction fronts develop and summarizes the notation convention followed in the analysis. In anticipation of application of the analysis to samples of metaperidotite from Val d'Efra, the domains are designated C, J, and I2 (as in Table 1; Figs. 3, 4). The steady-state value of reaction progress when a domain reaches equilibrium with the input fluid, ξ_{ss}, generally is different in each domain. The volume fraction of each domain is designated *VF*. Reaction fronts (F1, F2, F3) are numbered in the order that they are encountered downstream, beginning with the front closest to the inlet. After flow has occurred, reaction fronts F1, F2, and F3 lie at positions z(F1), z(F2), and z(F3). Between the inlet ($z = 0$) and z(F1), fluid composition is X°, the time-integrated flux is q°, and $\xi = \xi_{ss}$ in each domain. Between z(F1) and z(F2), ξ is zero in one domain (C) and is $0 < \xi^* < \xi_{ss}$ in the other two [ξ^*(F1,J) in domain J and ξ^*(F1, I2) in domain I2]. Between z(F2) and z(F3), ξ is zero in two domains (C, J) and is ξ^*(F2,I2) in the third (I2). Fluid composition on the upstream and downstream sides of F1 is $X^i(\mathrm{F1}) = X^\circ$ and X^{eq}(F1), respectively, where X^{eq}(F1) is the composition of fluid in equilibrium with reactants and products in all domains at F1. Fluid composition on the upstream and downstream sides of F2 is $X^i(\mathrm{F2}) = X^{eq}$(F1), and X^{eq}(F2), respectively. Fluid composition on the upstream and downstream sides of F3 is $X^i(\mathrm{F3}) = X^{eq}$(F2), and X^{eq}(F3), respectively. Time-integrated fluid flux on the upstream and downstream sides of F1 is $q^i(\mathrm{F1}) = q^\circ$ and q^i(F2), respectively. Time-integrated fluid flux on the upstream and downstream sides of F2 is q^i(F2) and q^i(F3), respectively. Time-integrated fluid flux on the upstream side of F3 is q^i(F3).

The decrease in time-integrated fluid flux across reaction front F1, caused by consumption of Δn_{CO_2} moles CO_2 and of Δn_{H_2O} moles H_2O by reaction (1), is computed from mass balance of CO_2:

$$X^{eq}(\mathrm{F1}) = \frac{X^\circ q^\circ - \Delta n_{CO_2}}{q^\circ - (\Delta n_{CO_2} + \Delta n_{H_2O})} = \frac{X^\circ q^\circ - (5/6)\Delta n}{q^\circ - \Delta n}, \tag{8}$$

where $\Delta n = \Delta n_{CO_2} + \Delta n_{H_2O}$. Considering that $q^i(\mathrm{F2}) = q^\circ - \Delta n$,

$$q^i(\mathrm{F2}) = q^\circ \frac{[6X^\circ - 5]}{[6X^{eq}(\mathrm{F1}) - 5]} \tag{9}$$

Similarly,

$$q^i(\mathrm{F3}) = q^\circ \frac{[6X^\circ - 5]}{[6X^{eq}(\mathrm{F2}) - 5]}. \tag{10}$$

The X_{CO_2} of fluid in equilibrium with reactants and products at F3, X^{eq}(F3), is the X_{CO_2} at which domain I2 begins reaction (X^{eq} when $\xi = 0$ in domain I2). Similarly, X^{eq}(F2) is X^{eq} when $\xi = 0$ in domain J, and X^{eq}(F1) is X^{eq} when $\xi = 0$ in domain C. Reaction progress in domain I2 when reaction begins in domain J, ξ^*(F2,I2), is the value of ξ in domain I2 when $X^{eq} = X^{eq}$(F2) (Fig. 4). Values of reaction progress in domains J and I2 when reaction begins in domain C, ξ^*(F1,J) and ξ^*(F1,I2), respectively, are the values of ξ in domains J and I2 when $X^{eq} = X^{eq}$(F1).

Following the derivation of Eq. 3 from Eq. 2 and considering Eqs. 8–10,

$$v(\mathrm{F3}) = \frac{z(\mathrm{F3})}{q^\circ} = \left\{\frac{X^{eq}(\mathrm{F2}) - X^{eq}(\mathrm{F3})}{[5 - 6X^{eq}(\mathrm{F3})][\xi^*(\mathrm{F2,I2})VF(\mathrm{I2})]}\right\}\frac{[6X^\circ - 5]}{[6X^{eq}(\mathrm{F2}) - 5]}, \tag{11}$$

$$v(\mathrm{F2}) = \frac{z(\mathrm{F2})}{q^\circ} = \left\{\frac{X^{eq}(\mathrm{F1}) - X^{eq}(\mathrm{F2})}{[5 - 6X^{eq}(\mathrm{F2})][\Delta\xi(\mathrm{F2,I2})VF(\mathrm{I2}) + \xi^*(\mathrm{F1,J})VF(\mathrm{J})]}\right\}\frac{[6X^\circ - 5]}{[6X^{eq}(\mathrm{F1}) - 5]}, \tag{12}$$

$$v(F1) = \frac{z(F1)}{q^\circ} = \frac{X^\circ - X^{eq}(\mathrm{F1})}{[5 - 6X^{eq}(\mathrm{F1})][\Delta\xi(\mathrm{F1,I2})VF(\mathrm{I2}) + \Delta\xi(\mathrm{F1,J})VF(\mathrm{J}) + \xi_{ss}(\mathrm{C})VF(\mathrm{C})]}, \tag{13}$$

Table 2 Input used for calculations of time-integrated fluid flux and positions of reaction fronts in model flow systems

Number domains	1	2	2	3	3	3
Number reaction fronts	1	1	2	1	2	3
VF(C)[a]	na	0.5	0.95	0.333	0.48	0.96
VF(J)[a]	na	na	na	0.333	0.48	0.02
VF(I2)[a]	1	0.5	0.05	0.333	0.04	0.02
X°[b]	0.3	0.3	0.3	0.3	0.3	0.3
X^{eq}(F1)[c]	0.1850	0.1850	0.1916	0.1850	0.1888	0.1916
X^{eq}(F2)[c]	na	na	0.1850	na	0.1850	0.1888
X^{eq}(F3)[c]	na	na	na	na	na	0.1850
ξ_{max}(C) (mol/cm^3)[d]	na	4.220×10^{-3}	4.220×10^{-3}	4.220×10^{-3}	4.220×10^{-3}	4.220×10^{-3}
ξ_{max}(J) (mol/cm^3)[d]	na	na	na	4.251×10^{-3}	4.251×10^{-3}	4.251×10^{-3}
ξ_{max}(I2) (mol/cm^3)[d]	4.972×10^{-3}	4.972×10^{-3}	4.972×10^{-3}	4.972×10^{-3}	4.972×10^{-3}	4.972×10^{-3}
ξ^*(F1,J) (mol/cm^3)[e]	na	na	na	0	0	0.881×10^{-3}
ξ^*(F1,I2) (mol/cm^3)[e]	na	0	1.894×10^{-3}	0	1.377×10^{-3}	1.894×10^{-3}
ξ^*(F2,I2) (mol/cm^3)[e]	na	na	0	na	0	1.377×10^{-3}
z(F1) chosen (m)[f]	18.00	18.00	18.00	18.00	18.00	12.00
q° theory (mol/cm^2)[g]	302.72	279.79	266.10	272.78	263.49	178.14
q° F-D (mol/cm^2)[g]	302.72	279.79	266.04	272.75	263.44	178.15
z(F2) theory (m)[h]	na	na	39.53	na	38.70	38.09
z(F2) F-D (m)[h]	na	na	39.39	na	38.64	38.06
z(F3) theory (m)[h]	na	na	na	na	na	52.33
z(F3) F-D (m)[h]	na	na	na	na	na	52.31

na not applicable

[a] Volume fraction of domains C, J, and I2

[b] X_{CO_2} of input fluid

[c] X_{CO_2} of fluid in equilibrium with reactants and products at reaction fronts F1, F2, and F3 from quadratic fits to ξ-X^{eq} relations computed from phase equilibria (Fig. 4)

[d] maximum possible value of reaction progress in domains C, J, and I2

[e] Value of reaction progress in domain J or I2 downstream from reaction front F1 or F2 (see Figs. 4 and 6)

[f] Position of reaction front F1 in the model flow system chosen for the basis of calculations

[g] Calculated time-integrated fluid flux to account for the displacement of reaction front F1 from $z = 0$ to the chosen position z(F1) using either theory (Eq. 3 or 13) or finite-difference calculations (F-D)

[h] Calculated positions of reaction fronts F2 and F3 for given value of q° using either theory (Eqs. 11 and 12) or finite-difference calculations (F-D)

where

$$\Delta\xi(\mathrm{F2,I2}) = \xi^*(\mathrm{F1,I2}) - \xi^*(\mathrm{F2,I2}), \quad (14)$$

$$\Delta\xi(\mathrm{F1,I2}) = \xi_{ss}(\mathrm{I2}) - \xi^*(\mathrm{F1,I2}), \quad (15)$$

and

$$\Delta\xi(\mathrm{F1,J}) = \xi_{ss}(\mathrm{J}) - \xi^*(\mathrm{F1,J}). \quad (16)$$

Equations 11–16 also apply to a two-domain medium if VF(I2) = 0. In this case, no more than two fronts develop, F1 and F2. If VF(I2) = VF(J) = 0, the equations refer to a homogenous one-domain medium in which only one front (F1) is possible with v(F1) specified by Eq. 13, the same as v(F) specified by Eq. 3 with ξ_{max} replaced by ξ_{ss}. The analysis can be extended to a medium composed of four or more domains by the addition of one $(\Delta\xi)(VF)$ term to the equations for each additional domain.

One, two, or three reaction fronts may occur in a three-domain medium depending on the volume fractions of the domains (refer to Figs. 4, 6; Table 2). A single front (F1) forms if v(F1) > v(F2) > v(F3), in turn, if VF(I2) is similar in magnitude to both VF(C) and VF(J) or larger. The velocity of the single front is specified by Eq. 13 with X^{eq}(F1) = X^{eq} in domain I2 at $\xi = 0$, $\Delta\xi$(F1,I2) = ξ_{ss}(I2), and $\Delta\xi$(F1,J) = ξ_{ss}(J). If v(F3) > v(F1) > v(F2), two fronts form (F1, F3). This occurs when VF(I2) is relatively small compared to both VF(C) and VF(J). The velocity of faster F3 is specified by Eq. 11 with X^{eq}(F2) = X^{eq} in domain J at

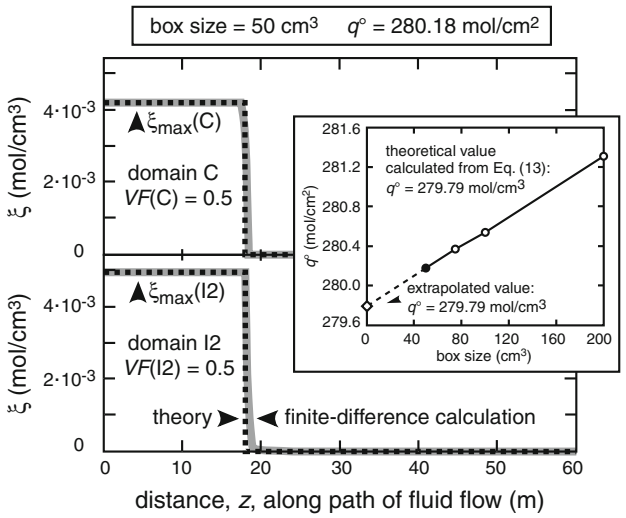

Fig. 7 Reaction front developed by infiltration of model metaperidotite, composed of two domains, with CO_2-H_2O fluid of composition $X_{CO_2} = 0.3$ and *P-T* conditions as in Fig. 5. The domains have initial compositions and abundances of minerals the same as samples C and I2 (Table 1), and each has a volume fraction of 0.5. The format of the diagram is the same as in Fig. 5. Theoretical value of q° was calculated from Eqs. 13 and 15 with $VF(J) = 0$, $\xi^*(F1,I2) = 0$, and $z(F1) = 18$ m (Table 2)

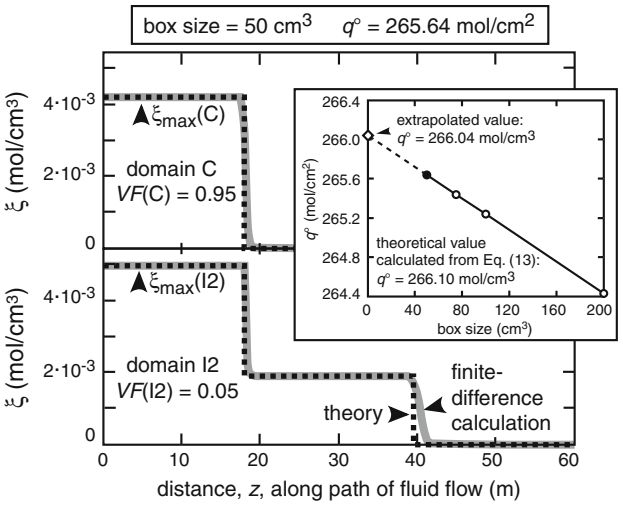

Fig. 8 Reaction fronts developed by infiltration of model metaperidotite, composed of two domains, with CO_2-H_2O fluid of composition $X_{CO_2} = 0.3$ and *P-T* conditions as in Fig. 5. Domains are the same as in Fig. 7 except the volume fractions of C and I2 are 0.95 and 0.05, respectively. The format of the diagram is the same as in Fig. 5. Theoretical value of q° calculated from Eqs. 13 and 15 with $VF(J) = 0$ and $z(F1) = 18$ m. Theoretical position of the faster reaction front in domain I2 was calculated from Eqs. 12 and 14 with $VF(J) = 0$ and $\xi^*(F2,I2) = 0$ (Table 2)

$\xi = 0$ and $X^{eq}(F3) = X^{eq}$ in domain I2 at $\xi = 0$. The velocity of slower F1 is specified by Eq. 13 with $X^{eq}(F1) = X^{eq}$ in domain J at $\xi = 0$, $\Delta\xi(F1,I2) = \xi_{ss}(I2) - \xi^*(F2,I2)$, and $\Delta\xi(F1,J) = \xi_{ss}(J)$. Three fronts develop when $VF(J)$ and $VF(I2)$ are small enough relative to $VF(C)$ that $v(F3) > v(F2) > v(F1)$.

Finite-difference model for reaction fronts in a heterogeneous medium

The finite-difference model for the calculation of the positions of reaction fronts in a heterogeneous medium is based on an extension of Eq. 4 to the case of a medium composed of p domains:

$$X^{eq}_{j,k} = \frac{\left(X^i_{j,k}\right)\left(\Delta q^i_{j,k}\right) - 5(z_{box})\sum_{i=1}^{p}\{[\Delta\xi(i)_{j,k}][VF(i)]\}}{\Delta q^i_{j,k} - 6(z_{box})\sum_{i=1}^{p}\{[\Delta\xi(i)_{j,k}][VF(i)]\}}. \quad (17)$$

Following the introduction of the *j*th fluid pulse into the *k*th box, $X^{eq}_{j,k}$ and the *p* values of $\Delta\xi(i)_{j,k}$ and $\xi(i)_{j,k}$ were calculated by solving $2p + 1$ equations: Eq. 17; *p* equations like Eq. 5, one for each domain i; and p equations like Eq. 6, one for each domain. Individual domains are not allowed to react if $X^{eq}_{j,k}$ is less than the X^{eq} at which the domain starts reaction ($\xi = 0$). Following attainment of mineral-fluid equilibrium in the box, the size of the increment of time-integrated flux was adjusted by the equivalent of Eq. 7:

$$\Delta q_{j,k} = \Delta q^i_{j,k} - 6(z_{box})\sum_{i=1}^{p}\{[\Delta\xi(i)_{j,k}][VF(i)]\}. \quad (18)$$

The process was then repeated in the same way as in the finite-difference model for a homogeneous medium.

Calculated reaction fronts produced by the disequilibrium flow mechanism

Equations 11–16 and the finite-difference method were used to compute reaction fronts in both two- and three-domain media composed of rocks modeled after three samples of metaperidotite (samples C, I2, and J, Table 1). Conditions of reaction (1) were taken as 645°C and 7 kbar. Input fluid has $X^\circ = 0.3$; therefore $\xi_{ss} = \xi_{max}$ in each domain (Fig. 4). Values used for the other terms in Eqs. 11–16 and all calculated results are listed in Table 2. The finite-difference calculations followed those for the homogenous medium (Fig. 5) in terms of box size, input fluid composition, and the increment of input time-integrated fluid flux.

Calculations for the two-domain model are based on samples C and I2 [$VF(J) = 0$]. Under circumstances in which two fronts develop, the first domain to react is I2, the one whose initial X^{eq} (Fig. 4) is further removed from X°. With reference to Eq. 15 and Table 2, $\xi^*(F1,I2) = 1.894 \times 10^{-3}$ mol/cm^3, the value of ξ in domain I2 at

$X^{eq} = 0.1916$ when domain C starts reaction (point b, Fig. 4). Using this and other values for variables that govern the 2-domain, 2-front model in Table 2, and substituting [1 − *VF*(I2)] for *VF*(C), the value of *VF*(I2) at which $v(F1) = v(F2)$ was computed by setting Eq. 12 equal to Eq. 13. The result is $VF(I2) = 0.108$. When $VF(I2) > 0.108$, $v(F1) > v(F2)$, and a single front (F1) develops. When $VF(I2) < 0.108$, $v(F1) < v(F2)$, and two fronts develop (F1, F2).

Calculations were carried out for a medium composed of two domains in which either one or two fronts develop (Table 2). Figure 7 illustrates the case of $VF(I2) = VF(C) = 0.5$ in which a single front is expected (F1). Figure 8 illustrates the case of $VF(I2) = 0.05$ and $VF(C) = 0.95$ in which two fronts are expected (F1, F2). The dashed lines represent the reaction front(s) predicted from theory. The slower reaction front F1 lies at the same position in both domains. When present, the faster front (F2) is confined to the I2 domain. For a displacement of the F1 reaction front 18 m from the inlet ($z = 0$), the time-integrated input fluid flux, $q°$, calculated from Eq. 13, is 279.79 mol/cm^2 in the case of one front (Fig. 7) and 266.10 mol/cm^2 in the case of two fronts (Fig. 8). Corresponding finite-difference calculations were carried out until ξ reached $\xi_{ss} = \xi_{max}$ in domain I2 in the box whose downstream end lies at 18 m. Results (gray curves) reproduce the theoretical predictions in Figs. 7 and 8 but with a small degree of broadening caused by numerical dissipation (cf. Fig. 5). The extrapolated values of $q°$ from the finite-difference calculations (insets to Figs. 7 and 8) in both cases agree with $q°$ calculated from Eq. 13 within the uncertainty of 0.06 mol/cm^2.

For $q° = 266.10$ mol/cm^2, the position of the faster F2 reaction front, $z(F2)$, is 39.53 m (Fig. 8, Table 2), calculated from Eq. 12. The preferred estimate of $z(F2) = 39.39$ m from the finite-difference calculations was taken as the position of the mid-point of F2 from computations for box sizes of 50 and 75 cm extrapolated to zero box size. Although the uncertainty in this estimate is difficult to evaluate, the difference between the value of $z(F2)$ from the finite-difference calculations and the value predicted from Eq. 12 is 0.14 m, less than half the smallest box size used in the finite-difference calculations, 0.5 m.

Calculations for the three-domain model are based on samples C, J, and I2. The first domain to react is I2, the second is domain J, and the third is domain C (Fig. 4). With reference conditions at which two fronts develop [Eqs. 15–16 and Table 2], $\xi^*(F1,J) = 0$, and $\xi^*(F1,I2) = 1.377 \times 10^{-3}$ mol/cm^3, the value of ξ in domain I2 at $X^{eq} = 0.1888$ when domain J starts reaction (point c, Fig. 4). Using these and other values for parameters that govern the 3-domain, 2-front model, substituting $VF(J) = VF(C) = [1\text{-}VF(I2)]/2$ in Eqs. 12 and 13, the value of

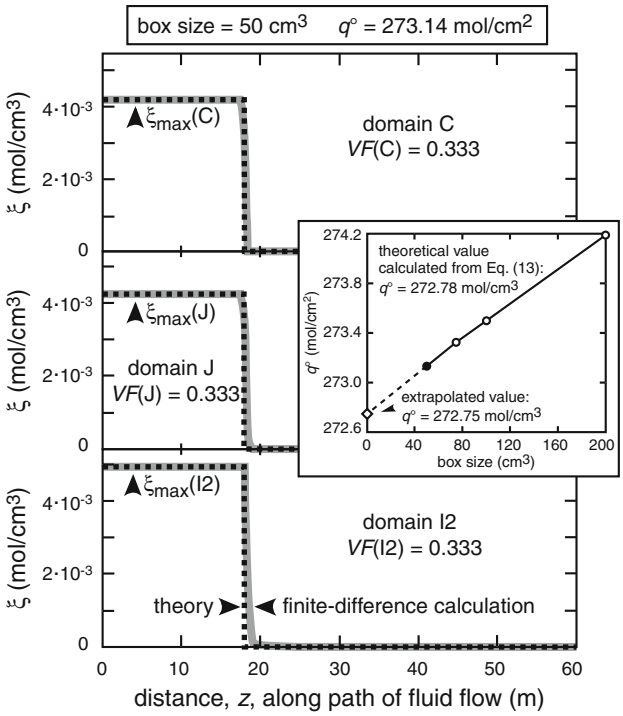

Fig. 9 Reaction front developed by infiltration of model metaperidotite, composed of three domains, with CO_2-H_2O fluid of composition $X_{CO_2} = 0.3$ and *P*-*T* conditions as in Fig. 5. The domains have initial compositions and abundances of minerals the same as samples C, I2, and J (Table 1), and each has a volume fraction of 0.333. The format of the diagram is the same as in Fig. 5. Theoretical value of $q°$ was calculated from Eqs. 13, 15, and 16 with $\xi^*(F1,I2) = \xi^*(F1,J) = 0$ and $z(F1) = 18$ m (Table 2)

VF(I2) at which $v(F2) = v(F3)$ was computed by setting Eq. 12 equal to Eq. 13. The result is $VF(I2) = 0.157$. When $VF(C) = VF(J)$ and $VF(I2) > 0.157$, $v(F1)$ is greater than $v(F2)$ and $v(F3)$, and a single front forms (F1). When $VF(I2) < 0.157$, $v(F2) > v(F1)$, and two fronts form (F1, F2).

With reference conditions at which three fronts develop (Table 2), $\xi^*(F1,J) = 0.881 \times 10^{-3}$ mol/cm^3, the value of ξ in domain J at $X^{eq} = 0.1916$ when domain C starts reaction (point a, Fig. 4); $\xi^*(F1,I2) = 1.894 \times 10^{-3}$ mol/cm^3, the value of ξ in domain I2 at $X^{eq} = 0.1916$; and $\xi^*(F2,I2) = 1.377 \times 10^{-3}$ mol/cm^3, the value of ξ in domain I2 at $X^{eq} = 0.1888$ when domain J starts reaction (point c, Fig. 4). Using these and other values for parameters that govern the 3-domain, 3-front model in Table 2, substituting $VF(J) = VF(I2)$ and $VF(C) = 1 - 2VF(I2)$ in Eqs. 11 and 12, the value of *VF*(I2) at which $v(F2) = v(F3)$ was computed by setting Eq. 11 equal to Eq. 12. The result is $VF(I2) = 0.062$. When $VF(I2) = VF(J) > 0.062$, $v(F1)$ is greater than both $v(F2)$ and $v(F3)$, and a single front develops (F1). When $VF(I2) = VF(J) < 0.062$, $v(F3) > v(F2) > v(F1)$ and three fronts develop (F1, F2, F3).

Calculations were carried out for a medium composed of three domains in which either one, two or three fronts

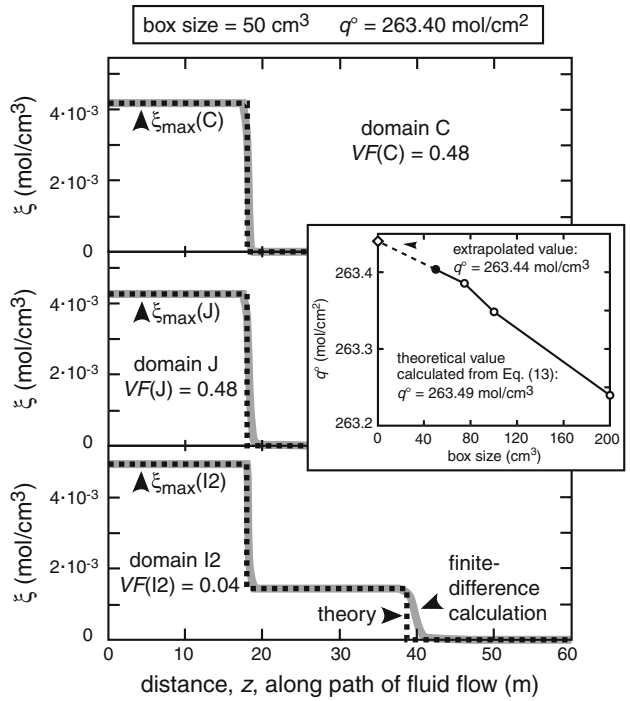

Fig. 10 Reaction fronts developed by infiltration of model metaperidotite, composed of three domains, with CO_2-H_2O fluid of composition $X_{CO_2} = 0.3$ and *P-T* conditions as in Fig. 5. Domains are the same as in Fig. 9 except the volume fractions of C, I2, and J are 0.48, 0.04 and 0.48, respectively. The format of the diagram is the same as in Fig. 5. Theoretical value of $q°$ was calculated from Eqs. 13, 15, and 16 with $\xi^*(F1,J) = 0$ and $z(F1) = 18$ m. Theoretical position of the faster reaction front in domain I2 was calculated from Eqs. 12 and 14 with $\xi^*(F1,J) = \xi^*(F2,I2) = 0$ (Table 2)

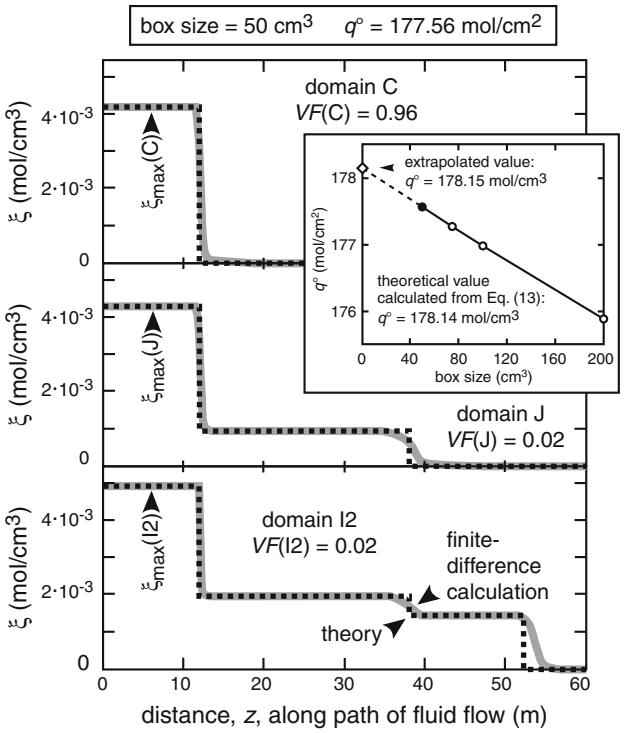

Fig. 11 Reaction fronts developed by infiltration of model metaperidotite, composed of three domains, with CO_2-H_2O fluid of composition $X_{CO_2} = 0.3$ and *P-T* conditions as in Fig. 5. Domains are the same as in Fig. 9 except the volume fractions of C, I2, and J are 0.96, 0.02 and 0.02, respectively. The format of the diagram is the same as in Fig. 5. Theoretical value of $q°$ was calculated from Eqs. 13, 15, and 16 with $z(F1) = 12$ m. Theoretical position of the fastest reaction front in domain I2 was calculated from Eq. 11. Theoretical position of the intermediate-speed reaction front in domains I2 and J was calculated from Eqs. 12 and 14

develop (Table 2). Figure 9 illustrates the case of $VF(I2) = VF(J) = VF(C) = 0.333$ in which a single front is expected (F1). Figure 10 illustrates the case of $VF(C) = VF(J) = 0.48$ and $VF(I2) = 0.04$ in which two fronts are expected (F1, F2). Figure 11 illustrates the case of $VF(C) = 0.96$ and $VF(I2) = VF(J) = 0.02$ in which three fronts are expected (F1, F2, F3). The dashed lines represent the reaction front(s) predicted from theory. The slowest reaction front F1 lies at the same position in all three domains. When present in domains I2 and J, the intermediate front (F2) lies at the same position in both domains. When it develops, the fastest front (F3) is confined to the I2 domain. The time-integrated input fluid flux required to displace the F1 reaction front 18 m from the inlet ($z = 0$) in the cases of one and two fronts was calculated from Eq. 13. Calculated values of $q°$ are 272.78 mol/cm^2 and 263.49 mol/cm^2, respectively (Figs. 9, 10; Table 2). The time-integrated input fluid flux required to displace the slowest F1 reaction front 12 m from the inlet ($z = 0$) in the case of three fronts, 178.14 mol/cm^2, was computed similarly (Fig. 11, Table 2). (The smaller 12 m displacement was chosen to keep the fastest F3 front within the same 60 m model flow system.) Corresponding finite-difference calculations were carried out until ξ reached $\xi_{ss} = \xi_{max}$ in domain I2 in the box whose downstream end lies at 18 m (Figs. 9, 10) or 12 m (Fig. 11). Results (gray curves) reproduce the theoretical predictions in Figs. 9, 10, and 11 but with some broadening, especially of the F2 and F3 fronts, caused by numerical dissipation. The extrapolated values of $q°$ from the finite-difference calculations (insets to Figs. 9, 10 and 11) agree in all cases with $q°$ calculated from Eq. 13 within uncertainty.

For $q° = 263.49$ mol/cm^2, the position of the faster F2 reaction front, z(F2) in Fig. 10, is 38.70 m from the inlet (Table 2), calculated from Eq. 12. For $q° = 178.14$ mol/cm^2, the position of the intermediate-speed F2 reaction front, z(F2), and of the fastest F3 reaction front, z(F3), in Fig. 11, are 38.09 m and 52.33 m, respectively (Table 2), calculated from Eqs. 11 and 12. The three corresponding estimates of the positions of the reaction fronts made from extrapolations of finite-difference calculations for box sizes of 50 and 75 cm to zero box size are 38.64, 38.06, and 52.31 m, respectively (Table 2). The difference between

the positions of the reaction fronts from the finite-difference calculations and those predicted from Eqs. 11 and 12 in all cases is <10 cm, less than half the smallest box size used in the finite-difference calculations.

Based on the theoretical analysis, the widespread occurrence of rocks containing reactants and products of an arrested decarbonation/dehydration (or carbonation/hydration) reaction that are fixed in composition is evidence that the mineral-fluid reaction occurred by the gradient flow mechanism rather than the disequilibrium flow mechanism (Ferry 1991). When minerals are solid solutions, however, the disequilibrium flow mechanism can also produce a widespread distribution of rocks with reactants and products ($0 < \xi < \xi_{max}$) in either or both of two circumstances. First, X° of the input fluid may be between the values corresponding to fluid-rock equilibrium when reaction begins and goes to completion, i.e., $\xi_{ss} < \xi_{max}$ (Fig. 4). Second, considering results in Figs. 8, 9, 10, and 11, $0 < \xi < \xi_{max}$ in some parts of the flow system, even when $\xi_{ss} = \xi_{max}$, if three requirements are met: (1) the flow medium is made up of numerous small domains that differ in chemical composition; (2) fluid composition is homogenized during metamorphism at a spatial scale larger than the size of individual domains; and (3) the volume fraction of at least some domains is very small. The three requirements are met in the case of the metaperidotite in Val d'Efra (Table 1, Ferry et al. 2005). Before the possibility can be further evaluated, however, the effect of solid solution and diffusion on mineral-fluid reactions driven by the gradient flow mechanism must be first evaluated.

Transport calculations: models of the gradient flow mechanism

The gradient flow reaction mechanism refers to the case in which the infiltrating fluid is everywhere in equilibrium with rock both at the inlet to the flow system and at all positions downstream. If there is a gradient in T and/or P along the flow path, mineral-fluid reactions inevitably occur as the flowing fluid adjusts its composition toward equilibrium under changing P-T conditions. If the fluid is a CO_2-H_2O solution and reactant and product minerals are fixed in composition, progress of a decarbonation/dehydration (or carbonation/hydration) reaction, and of reaction (1) in particular, at any position in the flow system is related to time-integrated fluid flux (q) at that position by:

$$q = \xi \frac{v_{CO_2} - X(v_{CO_2} + v_{H_2O})}{(\partial X/\partial z)} = \xi \frac{(6X-5)}{(\partial X/\partial z)} = \xi R, \qquad (19)$$

where $X = X_{CO_2}$ and $\partial X/\partial z$ is the gradient in X along the fluid flow path (Baumgartner and Ferry 1991). Considering Eq. 9 or 10,

$$q^\circ = q \frac{[v_{CO_2} - (v_{CO_2} + v_{H_2O})X]}{[v_{CO_2} - (v_{CO_2} + v_{H_2O})X^\circ]} = q \frac{(6X-5)}{(6X^\circ - 5)}$$
$$= \xi R \frac{(6X-5)}{(6X^\circ - 5)} = \xi R^\circ. \qquad (20)$$

Application of Eq. 20 to mineral-fluid reactions in which one or more of the reactants and products is a solid solution faces several complications. First, X, $\partial X/\partial z$, and R° are functions of ξ rather than constants. Second, if the flow medium is composed of multiple domains that differ in composition but equilibrate at all times with fluid of the same X, both ξ and R° depend on the volume fraction and ξ-X relations for each domain. Third, $\partial X/\partial z$ depends not just on the T and P gradients along the flow path (as is the case when minerals are fixed in composition), but also on $\partial\xi/\partial z$, the gradient in ξ along the flow path. Finite-difference calculations were carried out to identify simple ways that may be used to estimate q° from Eq. 20 even when minerals involved in the reaction are solid solutions and when the flow medium is composed of multiple domains.

In applications to the gradient flow reaction mechanism, the distance coordinate of the finite-difference model was expanded to 390 m. Values of $T = 645$°C and $P = 7$ kbar were assigned to the spatial position $z = 0$, and the inlet to the flow system was assigned to the position $z = -240$ m. Because most fluid flow during Barrovian regional metamorphism is believed to be oriented vertically upwards (e.g., Hanson 1992, 1997; Lyubetskaya and Ague 2009) along normal geothermal and lithostatic P gradients, $\partial T/\partial z$ and $\partial P/\partial z$ were chosen as −30°/km and −270 bars/km.

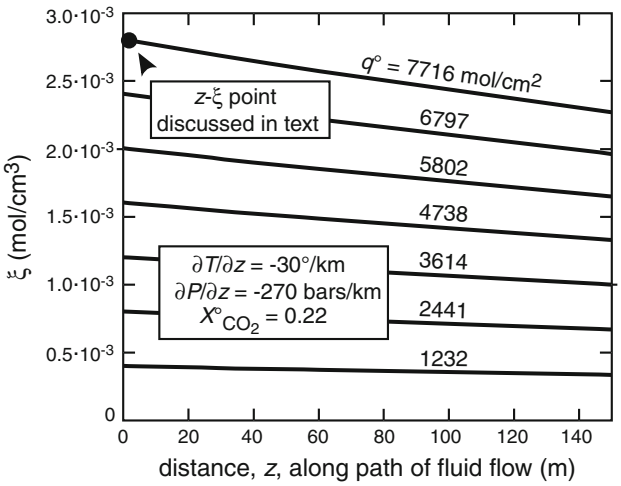

Fig. 12 Calculated variation of ξ with q° and z in the spatial portion of a finite-difference model for infiltration of model metaperidotite by CO_2-H_2O fluid in which reaction (1) is driven by the gradient flow mechanism. At $z = 0$, $T = 645$°C and $P = 7$ kbar. The T and P gradients along the flow path and the X_{CO_2} of the input fluid are given in the inset

Temperature, P, and ξ-X^{eq} relations (as in Fig. 4) were calculated from the T and P gradients and phase equilibria for domains I2 and C at 15-m intervals from $z = -240$ m to $z = +150$ m. The ξ-X^{eq} relations at each spatial position were fit to a quadratic function to simplify computations. The ξ-X^{eq} relations at intermediate positions were interpolated from the quadratic fits. The box size was chosen as 1 m, and the composition of input CO_2-H_2O fluid was taken as $X^\circ = 0.22$. Increments in q° introduced at the inlet to the flow system correspond to a volume of fluid 1% of the box size. Following input of an increment of q°, values of $X^{eq}_{j,k}$ and $\xi(i)_{j,k}$ for each of the p domains in each box were computed by solving 2p +1 equations, a single Eq. 17 and p Eqs. 5 and 6, one for each domain. The principal difference between these and the previous finite-difference calculations is that the ξ-X^{eq} relations for each domain are different in each of the boxes. Infiltration of the input fluid causes a single reaction front to form close to the inlet. Downstream from the front, rock, and fluid are in equilibrium at each spatial point. Continued progress of reaction (1) downstream from the reaction front is driven by flow along the T and P gradient.

Results of calculated ξ-z relations downstream from the reaction front for a homogeneous (one-domain) medium with composition the same as sample I2 (Table 1) are illustrated in Fig. 12. At each spatial point, for a given q°, the finite-difference calculations provided values of X^{eq}, $\partial X^{eq}/\partial z$, and R° as well as ξ. The results demonstrate that q° can be accurately calculated in the case when mineral reactants and products are solid solutions by:

$$q^\circ = \int_0^{\xi^f} R^\circ(\xi) d\xi, \tag{21}$$

where ξ^f is the final value of ξ at the spatial position z of interest. As an example, consider $\xi^f = 2.8 \times 10^{-3}$ mol/cm^3 at $z = 1.8$ m (black circle, Fig. 12). The value of $\xi^f = 2.8 \times 10^{-3}$ mol/cm^3 was chosen because it is slightly larger than the largest measured value of ξ in samples of metaperidotite from Val d'Efra (Table 1). From integration of ξ-R° relations at $z = 1.8$ m, $q^\circ = 7{,}737$ mol/cm^2 from Eq. 21. The value of q° from the finite-difference calculations for $\xi^f = 2.8 \times 10^{-3}$ mol/cm^3 at $z = 1.8$ m is 7,716 mol/cm^2, a difference of 0.27%. Calculations of q° from Eq. 21 successfully reproduce values from the finite-difference calculations within <0.3% for the entire range of z and ξ^f in Fig. 12.

Methods to calculate q° when the flow medium contains multiple domains, as well as reactants and products that are solid solutions, were evaluated by conducting a second set of finite-difference calculations in which the flow medium was composed of two domains corresponding to samples C and I2 (Table 1) with $VF(C) = VF(I2) = 0.5$. Taking the same example of $\xi^f(I2) = 2.8 \times 10^{-3}$ mol/cm^3 at $z = 1.8$ m, q° was calculated by:

$$q^\circ = \sum_{i=1}^{p} \left\{ VF(i) \int_0^{\xi^f(i)} R^\circ[\xi(i)] d\xi(i) \right\}, \tag{22}$$

where i refers to each of the $p = 2$ domains. The result (5,787 mol/cm^2) agrees with the value from the finite-difference calculations to four significant digits. Calculations of q° from Eq. 22 successfully reproduce values from the finite-difference calculations for the 2-domain flow medium within 0.3% for the entire range of z and ξ investigated.

In applications of Eqs. 21 and 22 to a given spatial position in a natural fossil fluid flow system, $\partial X/\partial z$ rigorously would be evaluated as:

$$\partial X/\partial z = (\partial X/\partial T)_{P,\xi}(\partial T/\partial z) + (\partial X/\partial P)_{T,\xi}(\partial P/\partial z) + (\partial X/\partial \xi)_{T,P}(\partial \xi/\partial z), \tag{23}$$

where $(\partial X/\partial T)_{P,\xi}$, $(\partial X/\partial P)_{T,\xi}$, and $(\partial X/\partial \xi)_{T,P}$ are the dependencies of X on T, P, and ξ, respectively, and $(\partial T/\partial z)$, $(\partial P/\partial z)$, and $(\partial \xi/\partial z)$ are the gradients in T, P, and ξ, respectively, along the flow path at the position of interest. When mineral reactants and products are fixed in composition, $(\partial X/\partial \xi)_{T,P}$ and hence the third term on the right-hand side of Eq. 23 is zero. An added complication in applying Eqs. 21 and 22 to rocks when reactants and products are solid solutions, therefore, is that $(\partial X/\partial \xi)_{T,P}(\partial \xi/\partial z)$ is both non-zero and difficult to evaluate without a numerical simulation of fluid flow and reaction. Because the largest of the three terms on the right-hand side of Eq. 23 is $(\partial X/\partial T)_{P,\xi}(\partial T/\partial z)$, the finite-difference calculations were used to determine whether the $(\partial X/\partial \xi)_{T,P}(\partial \xi/\partial z)$ term is small enough to be ignored. In the specific case of the gradient flow model for sample I2 in Fig. 12 and the point represented by the black circle, q° calculated from Eqs. 21 and 23 is 7,716 mol/cm^2 if the $(\partial X/\partial \xi)_{T,P}(\partial \xi/\partial z)$ term is included (as given above) and 8,293 mol/cm^2 if it is omitted. The difference (577 mol/cm^2) is 7.5% relative. The difference is smaller for all other ξ-z combinations in Fig. 12, decreasing to zero at all z as ξ [and $(\partial \xi/\partial z)$] decreases to zero. Similar calculations were made for the gradient flow model in a medium composed of two domains (C and I2). The difference between q° calculated from Eqs. 22 and 23 either ignoring or including the $(\partial X/\partial \xi)_{T,P}(\partial \xi/\partial z)$ term for the same ξ-z point represented by the black circle in Fig. 12 is 6,145–5,787 = 358 mol/cm^2, 6.2% relative. The difference is also smaller for all other ξ-z combinations in Fig. 12, decreasing to zero at all z as ξ [and $(\partial \xi/\partial z)$] decreases to zero. These calculations demonstrate that Eqs. 21 and 22 may be applied ignoring the $(\partial X/\partial \xi)_{T,P}(\partial \xi/\partial z)$ term, when mineral reactants and products

are solid solutions, without introducing great error. For comparison, ignoring $(\partial X/\partial \xi)_{T,P}(\partial \xi/\partial z)$ in the calculation of q°, relevant to carbonation of the metaperidotite at Val d'Efra, is equivalent to an error in the inferred temperature gradient along the flow path of ~ 2°/km or less.

Fluid flow in the Val d'Efra metaperidotite body during metamorphism

The goal of the study was to identify the mechanism(s) of reaction and set limits on the time-integrated fluid flux and input fluid composition during regional metamorphism of the metaperidotite body at Val d'Efra. The analysis considers model one-dimensional flow systems with bulk composition the same as the aggregate of the 13 samples in Table 1 that were collected along the ~ 1 m traverse in Fig. 3. At the dm scale, however, the model medium is heterogeneous, composed of 13 domains with the spatial dimensions and compositions of the 13 samples in Table 1 and Fig. 3. In technical terms, the representative elemental volume is the ~ 1 m traverse in Fig. 3, excluding samples I, L1, L2, and M. Fluid composition is assumed uniform at each time and spatial position in the flow system, as would occur if CO_2-H_2O interdiffusion homogenized fluid composition at the m-scale. All calculations assume mineral-fluid equilibrium during progress of reaction (1) and that the present level of exposure where the samples were collected experienced reaction (1) at $T = 645$°C and $P = 7$ kbar. The essential goal of the models is to reproduce measured values of ξ in Fig. 3 in all 13 domains at the spatial point(s) where $T = 645$°C and $P = 7$ kbar. In addition, the models make quantitative predictions about q° and about reaction progress (and hence modes and mineral compositions) at all other spatial points in the model flow system.

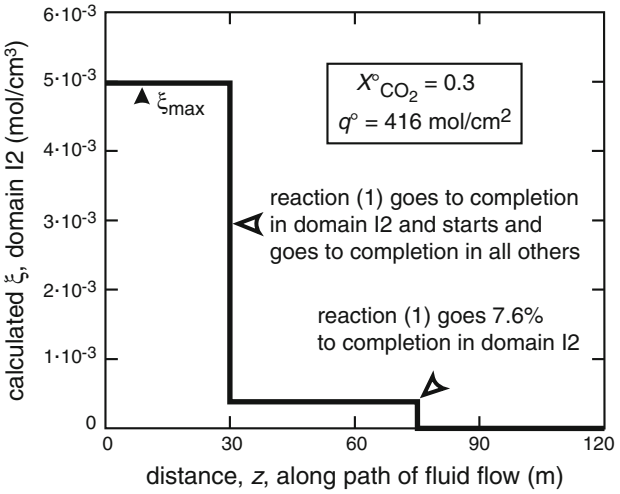

Fig. 13 Calculated variation of ξ in sample/domain I2 as a function of distance along the flow path predicted from a one-dimensional, 13-domain model for infiltration of the metaperidotite body at Val d'Efra by CO_2-H_2O fluid with $X_{CO_2} = 0.3$ and constant $T = 645$°C and $P = 7$ kbar. The domains have volume fractions and initial compositions and abundances of minerals the same as the samples in Table 1. The value of q° was calculated from the equivalent of Eq. 13 for a 13-domain medium and $z(\text{F1}) = 30$ m. The model predicts the development of only two reaction fronts: a faster front at which reaction (1) goes 7.6% to completion in domain I2, and a slower front at which reaction (1) goes to completion in domain I2 and starts and goes to completion in all the other domains. The model fails to predict observed values of ξ in any of the samples in Table 1

Disequilibrium flow reaction mechanism

The occurrence of reactants and products of reaction (1) along the traverse ($0 < \xi < \xi_{max}$) could have developed by the disequilibrium flow reaction mechanism (analogous to the region $z = 12$–38 m in Fig. 11). To parallel the calculations summarized in Figs. 7, 8, 9, 10, 11, the possibility was first quantitatively evaluated by a model of isothermal, isobaric infiltration of metaperidotite at 645°C and 7 kbar by a fluid with $X^\circ = 0.3$. In this case, $\xi_{ss} = \xi_{max}$ in all domains. Equations like 11–16 for a 13-domain model were developed with data in Table 1 for each domain. The volume fraction of each domain is considered half the sum of the separation of the corresponding sample from its nearest neighbors along the traverse (or separation of the samples at the ends of the traverse from their nearest neighbor) divided by the length of the traverse. Despite the large number of domains, only a two-front flow system develops governed by analogs to Eqs. 12 and 13. Calculated results are illustrated in Fig. 13 for a displacement of the slower reaction front of 30 m, comparable to the size of the metaperidotite body (Fig. 1). The value of q° is 416 mol/cm^2, calculated from the 13-domain equivalent of Eq. 13. Calculations were extended to a spatial scale larger than the metaperidotite body to characterize the entire model flow system. At the faster moving front ($z = 75.1$ m), reaction (1) only occurs in sample/domain I2 where it goes 7.6% to completion ($\xi = 0.38 \times 10^{-3}$ mol/cm^3). Reaction (1) goes to completion in domain I2, and the reaction starts and goes to completion in all the other 12 domains at the slower moving front ($z = 30$ m). Regardless of q°, the predicted distribution of reaction progress in the flow system is either no reaction in all domains, partial reaction in domain I2 and no reaction in all the others, or complete reaction in all domains. Because these predicted distributions are not observed in the metaperidotite, disequilibrium flow with an input of CO_2-H_2O fluid with $X^\circ = 0.3$ did not occur.

Calculations similar to those summarized in Fig. 13 were explored considering values of $X^\circ \neq 0.3$. For all

values of $X^\circ > 0.196$, calculated values of ξ_{ss} in each domain upstream from the slowest reaction front are greater than those measured (Fig. 3 and Table 1). For all values of $X^\circ < 0.196$, calculated values of ξ_{ss} in each domain upstream from the slowest reaction front are smaller than those measured. Regardless whether $X^\circ > 0.196$ or $X^\circ < 0.196$, calculated values of ξ downstream from the slowest reaction front additionally fail to reproduce measured values in all domains at a single spatial point. When $X^\circ = 0.196$, however, values of ξ_{ss} are identical to measured values and are developed everywhere in the model flow system upstream from the slowest reaction front. Calculated values of ξ downstream from the slowest front, therefore, are less than measured values in all domains. The insight that emerges from this analysis is that the infiltrating fluid that carbonated the peridotite body during regional metamorphism must have had composition $X^\circ = 0.196$ (provided reaction occurred at 645°C and 7 kbar).

The explanation why only a value of $X^\circ = 0.196$ reproduces all measured values of ξ in Table 1 is the following. Given the initial amounts and compositions of minerals in each of the 13 domains prior to reaction (Table 1), the weighted mean olivine composition ($X_{fo} = 0.888$) is reproduced exactly when ξ is the same as the measured value in the domain. The X_{CO_2} of CO_2-H_2O fluid in equilibrium with olivine ($X_{fo} = 0.888$), talc, and magnesite at 645°C and 7 kbar is 0.196. Equilibration of each domain with fluid with $X_{CO_2} = 0.196$, therefore, results in both olivine with $X_{fo} = 0.888$ and ξ identical to measured values (e.g., samples/domains C, I2, and J in Fig. 4).

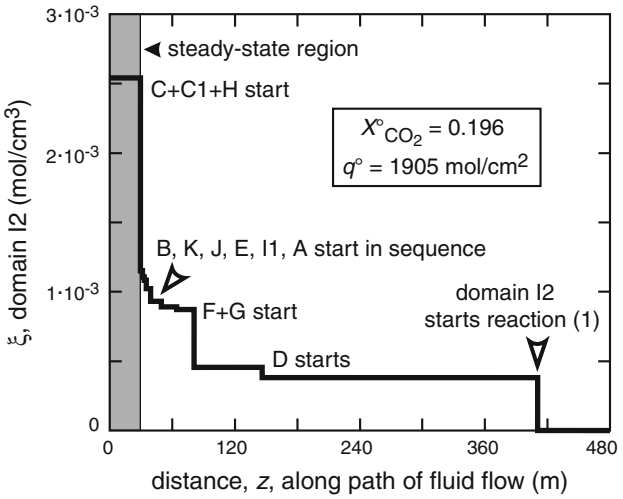

Fig. 14 Calculated variation of ξ in sample/domain I2 as a function of distance along the flow path predicted from a theoretical one-dimensional, 13-domain model for infiltration of the metaperidotite body at Val d'Efra by CO_2-H_2O fluid. Calculations of ξ and q° are the same as for Fig. 13 except that the input fluid has $X_{CO_2} = 0.196$. The model predicts the development of 10 reaction fronts. Upstream from the slowest reaction front (*gray region*), fluid has $X_{CO_2} = 0.196$ and calculated ξ for domain I2 is the same within error as the measured value (Fig. 4, Table 1)

To estimate the minimum value of q° involved in carbonation of the metaperidotite, a calculation like the one summarized in Fig. 13 was made but with $X^\circ = 0.196$. Applying equations like 11–16 to an isothermal, isobaric 13-domain flow system, a 10-front flow system develops. The system is best displayed by ξ(I2) as a function of distance along the flow path because it is the first sample/domain to begin reaction and continues to react as all the other domains join in later. Results are illustrated in Fig. 14 for $q^\circ = 1{,}905$ mol/cm^2 that displaces the slowest moving reaction front 30 m, a distance comparable to the size of the metaperidotite body. Model calculations were extended to a spatial scale much larger than the dimensions of the metaperidotite body to characterize the entire model flow system. The fastest reaction front develops only in domain I2, followed by the other nine fronts at which reaction starts in domain D; then in domains F and G together; and then, in sequence, domains B, K, J, E, I1, and A. The last domains to begin reaction are C, C1, and H, and they begin reaction together. Upstream from the slowest reaction front, the flow system is in a steady state in which $\xi(\text{I2}) = 2.52 \times 10^{-3}$ mol/cm^3 (Fig. 14), the measured value in the corresponding sample (Table 1). Values of $\xi = \xi_{ss}$ in the model flow system also match measured values in all the other domains upstream from the slowest reaction front but at no other spatial positions downstream. Any value of $q^\circ > 1{,}905$ mol/cm^2 would also produce the observed values of ξ in Table 1 at $z \leq 30$ m.

Although the measured values of ξ in Fig. 3 and Table 1 can be reproduced by the disequilibrium flow mechanism alone with $X^\circ = 0.196$, $q^\circ \geq 1{,}905$ mol/cm^2, and isothermal and isobaric conditions along the flow path (Fig. 14), such a model is not realistic. Except for implausibly special flow paths, fluid flow along gradients in T and/or P is inevitable during regional metamorphism. The potential effects of the gradient flow mechanism in driving reaction (1), therefore, must be considered as well.

Gradient flow reaction mechanism

The ubiquitous occurrence of samples that contain reactants and products of reaction (1) alternatively can be explained the gradient flow reaction mechanism. The required q° can be computed from Eq. 22 and the data in Table 1. The values of $\xi^f(i)$ are the measured values of ξ for each sample. The $R^\circ(\xi)$ functions were taken as cubic fits of R° to ξ in each sample. The $(\partial X/\partial z)$ used in calculation of R° for each sample was evaluated assuming T and P gradients of −30°C/km and −270 bars/km along the flow path (vertical upward flow) and that $(\partial X/\partial \xi)_{T,P}(\partial \xi/\partial z) = 0$.

Applying Eq. 22, $q^\circ = 4{,}232$ mol/cm^2 at the position in the flow system where $T = 645$°C and $P = 7$ kbar. If the input fluid composition is $X^\circ = 0.196$, any value of $q^\circ \geq 4{,}232$ mol/cm^2 reproduces the measured values of ξ in Table 1 at that same spatial point. By analogy with the simple one- and two-domain models of the gradient flow mechanism, rigorous evaluation of $(\partial X/\partial\xi)_{T,P}(\partial\xi/\partial z)$ would result in a value of q° smaller by no more than 6–8%.

In order to reproduce the measured value of ξ in all samples at a point in the flow system where $T = 645$°C and $P = 7$ kbar, the composition of the input fluid at the inlet to the flow system upstream must be $X^\circ = 0.196$. If $X^\circ < 0.196$, ξ values are smaller than those in Table 1 for all values of q°. Fluid with $X^\circ \geq 0.196$, however, will be out of equilibrium with reactant minerals at the start of reaction at any realistic position of the inlet upstream. A reaction front then develops controlled by the disequilibrium flow mechanism. Carbonation and hydration of the metaperidotite body, therefore, must be the result of both the gradient flow and disequilibrium flow mechanisms acting in concert.

Combined action of the disequilibrium and gradient flow mechanisms

Neither the gradient flow nor the disequilibrium flow mechanism was the sole driving force of reaction (1) in the metaperidotite body in Val d'Efra. The gradient flow mechanism acting alone is impossible because a value of $q^\circ = 4{,}232$ mol/cm^2 is required to reproduce all ξ values the same as those in Table 1. If $X^\circ = 0.196$, however, a reaction front, like the slowest front in Fig. 14, would have already swept through the ~30-m-diameter metaperidotite body [this would have occurred at a much lower value of $q^\circ \approx 1{,}905$ mol/cm^2 (Fig. 14)]. If $X^\circ > 0.196$, a reaction front like the slowest one in Fig. 14 would have swept through the metaperidotite even more rapidly and produced ξ values greater than those in Table 1 (e.g., Fig. 13). A value of $X^\circ < 0.196$ is impossible because reactive fluid flow then produces ξ values at 645°C and 7 kbar less than the measured values in Table 1 no matter what the value of q°. On the other hand, the disequilibrium flow mechanism could have acted alone only in the implausible circumstance of fluid flow in a direction along which $\partial X/\partial z = 0$ exactly (Eq. 19).

The preferred model for coupled fluid flow and mineral reaction in the metaperidotite, therefore, combines the effects of the disequilibrium and gradient flow mechanisms. The model flow medium is composed of 13 domains that correspond to the 13 samples in Table 1. Gradients in T and P along a vertical, upward flow path were taken as −30°C/km and −270 bars/km, and $(\partial X/\partial\xi)_{T,P}(\partial\xi/\partial z)$ was assumed zero. To reproduce the measured values of ξ in Table 1, fluid with $X^\circ = 0.196$ was introduced at the inlet to the flow system. The distance coordinate, z, was defined by assigning $T = 645$°C and $P = 7$ kbar at the position $z = 30$ m that corresponds to the present level of exposure of the metaperidotite body. The inlet at $z = 0$ then corresponds to the buried lower contact of the metaperidotite upstream. To characterize a large portion of the model fluid flow system, the spatial dimension of the calculations was extended for a distance much larger than the size of the metaperidotite body. The downstream end of the flow system lies at $z = 3{,}234$ m where, with decreasing T and P, reaction (1) becomes metastable with respect to a carbonation/hydration reaction that converts olivine to serpentine and magnesite rather than talc and magnesite. Twelve broad reaction fronts develop by the gradient flow reaction mechanism. The downstream tip of the each broad reaction front corresponds to the spatial position at which reaction (1) begins in each sample/domain. Proceeding

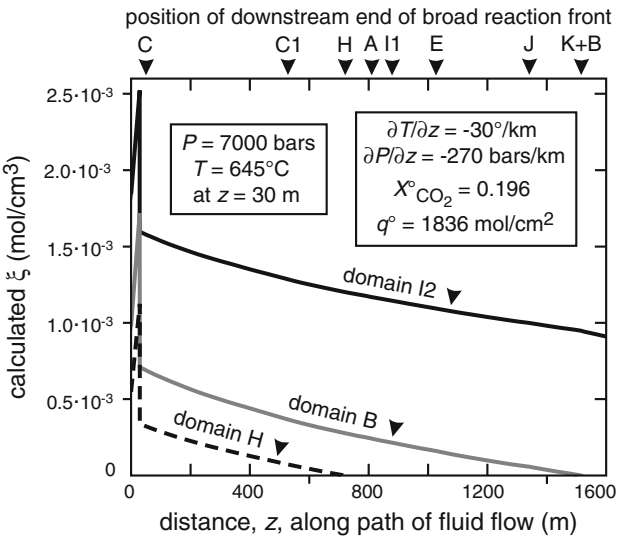

Fig. 15 Calculated variation of ξ in samples/domains I2 (*black solid curve*), B (*gray solid curve*), and H (*dashed black curve*) as a function of distance along the flow path predicted from a theoretical one-dimensional, 13-domain model for infiltration of the metaperidotite body at Val d'Efra by CO_2-H_2O fluid with $X_{CO_2} = 0.196$ and $q^\circ = 1{,}836$ mol/cm^2. Calculations differ from those in Fig. 14 by considering gradients in T and P along the flow path the same as in Fig. 12; $T = 645$°C and $P = 7$ kbar at $z = 30$ m. The model predicts the development of 8 broad reaction fronts, driven by the gradient flow mechanism, where 9 of the 13 domains start reaction (locations shown by *arrowheads* at top of figure). Broad reaction fronts for domains I2, D, F, and G lie beyond the end of the model flow system, off scale at 3,234 m. The model further predicts a single sharp reaction front at $z = 30$ m, driven by the disequilibrium flow mechanism, where ξ abruptly increases to values of ξ_{ss} that correspond to equilibrium of all domains with the input fluid (cf. Fig. 4). Calculated values of ξ at $z = 30$ m for all 13 domains are the same within error as the measured values (Table 1). Not visible at the scale of the figure is a discontinuity in slope along each broad reaction front where a new domain starts reaction

upstream, these are, in order, start of reaction in domains I2, D, F, and G in sequence; then K and B together; then J, E, I1, A, H, C1, and C in sequence. Upstream from the broad reaction fronts, a single sharp reaction front develops by the disequilibrium flow mechanism at which ξ abruptly increases in each domain to ξ_{ss}. When the sharp reaction front reaches the position $z = 30$ m, values of ξ_{ss} for every domain match the measured values in Fig. 3 and Table 1. The value of q° for the displacement of the sharp reaction front 30 m from the inlet to the flow system and values of ξ in each domain immediately downstream from the sharp reaction front were calculated by simultaneously solving Eqs. 11–16 and 22, modified for a 13-domain flow system with a gradient in T and P along the flow path, and utilizing the essentially linear relationship among values of ξ in the domains at all times and at each spatial point in the flow system. The value of ξ in each domain then was computed at each spatial point between the position of the sharp reaction front at $z = 30$ m and the end of the flow system at $z = 3{,}234$ m from Eq. 22.

The value of q° is 1,836 mol/cm^2, similar to the value predicted by the model of isothermal, isobaric disequilibrium flow (Fig. 14). Calculated q° would be no more than several percent smaller if $(\partial X/\partial\xi)_{T,P}(\partial\xi/\partial z)$ were rigorously evaluated rather than assumed to be zero. For $q^\circ = 1{,}836$ mol/cm^2, the tips of the broad reaction fronts for domains I2, D, F, and G lie at $z > 3{,}234$ m, beyond the downstream end of the model flow system. The tips of the broad reaction fronts in the other 9 domains (where ξ in the relevant domain goes to zero) lie in the range $z = 50$–$1{,}516$ m (Fig. 15). Calculated values of ξ along the flow path for representative domains H, B, and I2 are illustrated in Fig. 15. The increase in the ξ_{ss} values in the domains in the range $z = 0$–30 m results from the dependence of ξ_{ss} on X^{eq}, and hence on P, T, and distance along the flow path. At $z = 30$ m, for $q^\circ = 1{,}836$ mol/cm^2, the proportion of reaction driven by the gradient flow mechanism (prior to arrival of the sharp reaction front) varies in each domain from 2% in domain C (that begins reaction last) to 63% in domain I2 (that begins reaction first). For the 13-domain flow system as a whole, 42% of reaction (1) is driven by the gradient flow mechanism and 58% by the disequilibrium flow mechanism (when the sharp reaction front arrives at $z = 30$ m).

Discussion

The preferred estimated $q^\circ = 1{,}836$ mol/cm^2 is a lower bound for Barrovian regional metamorphism in Val d'Efra because both the sharp reaction front and the broad reaction fronts swept entirely through the ~30-m-diameter metaperidotite body. In a larger body, one or more reaction fronts could have been preserved, and the estimated displacement of the front(s) used to calculate q° exactly. The estimate of q° has additional uncertainties that can be evaluated qualitatively. Reaction (1) is not stable at $T > 645$°C at 7 kbar. If the T at which reaction (1) occurred was <645°C, the value of q° would be greater with q° increasing with decreasing T. If the infiltrating fluid contained dissolved salts, q° would be greater with q° increasing with increasing salinity (Ferry and Gottschalk 2009). The maximum decrease in CO_2 content that the infiltrating fluid can experience during reaction (1) is when the input fluid fully equilibrates with the rock. If mineral-fluid equilibrium was not attained, then even more input fluid would be required to explain the degree of carbonation of the metaperidotite recorded by the measured values of ξ. Regardless of the uncertainties, a lower bound on time-integrated fluid flux of 1,836 mol/cm^2 at the Val d'Efra locality is not unusually large. It is consistent with the range of q° values inferred for Barrovian regional metamorphic terrains worldwide (Ferry and Gerdes 1998).

The preferred model of coupled fluid flow and mineral reaction for the metaperidotite body in Val d'Efra makes predictions of how ξ should change along the flow path (Fig. 15). Unfortunately, the exposure of the metaperidotite is inadequate to test those predictions. In a larger, better-exposed metaperidotite body, a map of the spatial distribution of ξ in three dimensions would constrain the direction of fluid flow as well as X°, q°, and the mechanisms(s) of reaction.

Most importantly, results of this study point to the resolution of a longstanding paradox in the study of reactive fluid flow during regional metamorphism. Widespread occurrences of coexisting reactants and products of decarbonation/dehydration reactions are common in regional metamorphic terrains, and they have been interpreted as evidence of reactions driven by the gradient flow mechanism with fluid flow in the direction of increasing T (e.g., Baumgartner and Ferry 1991; Ferry 1992, 1994). Simple hydrodynamic models of regional metamorphism, however, normally predict fluid flow vertically upward in the direction of decreasing T (Hanson 1992, 1997; Lyubetskaya and Ague 2009). More recent models have predicted that up-T fluid flow may occur around synmetamorphic plutons (Lyubetskaya and Ague 2010) or when fluid transport occurs as porosity waves (Connolly 2010). A more general conciliation of the widespread spatial distribution of reactants and products of decarbonation/dehydration reactions with metamorphic fluid dynamics emerges from this study. If mineral reactants and products are solid solutions, if the flow medium is composed of numerous small domains with different chemical compositions, and if the composition of metamorphic fluid is homogenized by diffusion of CO_2 and H_2O perpendicular

to the flow direction over a spatial scale larger than the size of the domains, then a widespread occurrence of reactants and products may be produced by the disequilibrium flow mechanism, with or without a contribution from the gradient flow mechanism, even if fluid flow is in the direction of decreasing *T*.

Acknowledgments Research was supported by grants EAR-0635608 and EAR-1118713 from the U.S. National Science Foundation. We thank Jay Ague for his thoughtful review of the paper.

References

Ague JJ (2000) Release of CO_2 from carbonate rocks during regional metamorphism of lithologically heterogeneous crust. Geology 28:1123–1126

Ague JJ (2002) Gradients in fluid composition across metacarbonate layers of the Wepawaug Schist, Connecticut, USA. Contrib Mineral Petrol 143:38–55

Ague JJ (2003) Fluid flow in the deep crust. In: Rudnick RL (ed), Holland HD, Turekian KK (exec eds) Treatise on geochemistry. Elsevier, Oxford, pp 195–228

Ague JJ, Rye DM (1999) Simple models of CO_2 release from metacarbonates with implications for interpretation of directions and magnitudes of fluid flow in the deep crust. J Petrol 40: 1443–1462

Baumgartner LP, Ferry JM (1991) A model for coupled fluid-flow and mixed-volatile mineral reactions with applications to regional metamorphism. Contrib Mineral Petrol 106:273–285

Berman RG (1988) Internally-consistent thermodynamic data for minerals in the system Na_2O-K_2O-CaO-MgO-FeO-Fe_2O_3-Al_2O_3-SiO_2-TiO_2-H_2O-CO_2. J Petrol 29:445–522

Bickle MJ, Chapman HJ, Ferry JM, Rumble D III, Fallick AE (1997) Fluid flow and diffusion in the Waterville limestone, south-central Maine: constraints from strontium, oxygen and carbon isotope profiles. J Petrol 38:1489–1512

Connolly JAD (2010) The mechanics of metamorphic fluid expulsion. Elements 6:165–172

Cook SJ, Bowman JR (2000) Mineralogical evidence for fluid-rock interaction accompanying prograde contact metamorphism of siliceous dolomites: Alta stock aureole, Utah, USA. J Petrol 41:739–757

Evans BW, Trommsdorff V (1974) Stability of enstatite + talc, and CO_2-metasomatism of metaperidotite, Val d'Efra, Lepontine Alps. Am J Sci 274:274–296

Ferry JM (1991) Dehydration and decarbonation reactions as a record of fluid infiltration. Miner Soc Am Rev Miner 26:351–393

Ferry JM (1992) Regional metamorphism of the Waits River Formation, eastern Vermont: delineation of a new type of giant metamorphic hydrothermal system. J Petrol 33:45–94

Ferry JM (1994) Overview of the petrologic record of fluid flow during regional metamorphism in northern New England. Am J Sci 294:905–988

Ferry JM (2007) The role of volatile transport by diffusion and dispersion in driving biotite-forming reactions during regional metamorphism of the Gile Mountain Formation, Vermont. Am Miner 92:1288–1302

Ferry JM, Gerdes ML (1998) Chemically reactive fluid flow during metamorphism. Ann Rev Earth Planet Sci 26:255–287

Ferry JM, Gottschalk M (2009) The effect of salinity on infiltration-driven contact metamorphism of carbonate rocks. Contrib Mineral Petrol 158:619–636

Ferry JM, Wing BA, Rumble D (2001) Formation of wollastonite by chemically reactive fluid flow during contact metamorphism, Mt. Morrison pendant, Sierra Nevada, California. USA. J Petrol 42: 1705–1728

Ferry JM, Wing BA, Penniston-Dorland SC, Rumble D (2002) The direction of fluid flow during contact metamorphism of siliceous carbonate rocks: new data for the Monzoni and Predazzo aureoles, northern Italy, and a global review. Contrib Miner Petrol 142:679–699

Ferry JM, Rumble D III, Wing BA, Penniston-Dorland SC (2005) A new interpretation of centimetre-scale variations in the progress of infiltration-driven metamorphic reactions: case study of carbonated metaperidotite, Val d'Efra, Central Alps, Switzerland. J Petrol 46:1725–1746

Hanson RB (1992) Effects of fluid production on fluid flow during regional and contact metamorphism. J Metam Geol 10:87–97

Hanson RB (1997) The hydrodynamics of regional metamorphism due to continental collision. Econ Geol 92:880–891

Hofmann A (1972) Chromatographic theory of infiltration metasomatism and its application to feldspars. Am J Sci 272:69–90

Kerrick DM, Jacobs GK (1981) A modified Redlich-Kwong equation for H_2O, CO_2, and H_2O-CO_2 mixtures at elevated pressures and temperatures. Am J Sci 281:735–767

Lichtner PC, Carey JW (2006) Incorporating solid solutions in reactive transport equations using a kinetic discrete-composition approach. Geochim Cosmochim Acta 70:1356–1378

Lyubetskaya T, Ague JJ (2009) Modeling the magnitudes and directions of regional metamorphic fluid flow in collisional orogens. J Petrol 50:1505–1531

Lyubetskaya T, Ague JJ (2010) Modeling metamorphism in collisional orogens intruded by magmas: II. fluid flow and implications for Barrovian and Buchan metamorphism, Scotland. Am J Sci 310:459–491

Penniston-Dorland SC, Ferry JM (2006) Development of spatial variations in reaction progress during regional metamorphism of micaceous carbonate rocks, northern New England. Am J Sci 306:475–524

Winslow NW (2009) Fluid flow, reaction progress and solid solution in lithologically layered porous media. PhD Thesis, Johns Hopkins University